

PALACKÝ UNIVERSITY OLOMOUC



Faculty
of Science

Department of Optics

Quantum CZ gate with weak coupling

Diploma thesis

Author:

Robert Stárek

Field of study:

Optics and optoelectronics

Supervisor:

Mgr. Michal Mičuda, Ph.D.

Consultant:

Mgr. Miroslav Ježek, Ph.D.

UNIVERZITA PALACKÉHO V OLOMOUCI



Přírodovědecká
fakulta

Katedra optiky

Kvantové CZ hradlo se slabou vazbou

Diplomová práce

Autor:

Robert Stárek

Studijní obor:

Optika a optoelektronika

Vedoucí práce:

Mgr. Michal Mičuda, Ph.D.

Konzultant:

Mgr. Miroslav Ježek, Ph.D.

Abstract

We propose and experimentally demonstrate a scheme for conditional implementation of a maximally entangling quantum controlled-Z gate between two qubits whose coupling can be arbitrarily weak. We show that the weak inter-qubit coupling can be enhanced by quantum interference. Both before and after the inter-qubit interaction, one of the qubits is coherently coupled to an auxiliary quantum level, and finally it is projected back onto the qubit subspace. This procedure enhances the inter-qubit interaction strength although the coupling to auxiliary quantum level can be considered as a local bypass that allows the qubit to partly avoid the interaction with the other qubit.

We experimentally demonstrate our scheme using a linear optical setup with weak interferometric coupling between single-photon qubits. In our experiment, we utilize time-correlated photon pairs generated in the process of spontaneous parametric downconversion and we exploit their polarization and spatial degrees of freedom to implement the quantum bypass. We characterize the performance of our scheme by measuring the Hofmann lower bound on quantum gate fidelity for various strengths of coupling to the auxiliary mode. At the optimal operating point where the fidelity and success probability are maximized we perform a full quantum process tomography of the quantum control-Z gate to prove that the control-Z process was restored.

Keywords

quantum information, control-Z gate, Hofmann bound, Mach-Zehnder interferometer

Abstrakt

Navrhli jsme a pomocí lineární kvantové optiky experimentálně ověřili metodu podmíněné implementace kvantového maximálně entanglujícího control-Z hradla, operujícího na libovolně slabě vázaných kvantových bitech. Naše metoda je založena na obcházení interakce slabě vázaných kvantových bitů pomocí koherentního navázání a následného vyvázání jednoho kvantového bitu do pomocného módu. Po interakci je pomocný mód promítnut zpět do podprostoru původního kvantového bitu. Takto je dosaženo zesílení interakce mezi slabě vázanými kvantovými bity, přestože vazba do pomocného módu je lokální operací.

Experiment využívá časově korelované páry fotonů, které jsou generované pomocí spontánní parametrické sestupné frekvenční konverze. Pro kódování jednotlivých kvantových bitů se využívá prostorových a polarizačních módů fotonů. Slabá vazba mezi fotony, která běžně neumožňuje vytvoření control-Z hradla, je zprostředkována pomocí děliče svazku. Metoda je charakterizována svojí účinností a pomocí měření Hofmannovy dolní meze fidelity procesu pro různé síly vazby do pomocného módu. V optimálním režimu, kde dosahuje fidelita procesu a pravděpodobnost úspěšné operace svého maxima, je hradlo charakterizováno úplným tomografickým měřením.

Klíčová slova

kvantové zpracování informace, control-Z hradlo, Hofmannova mez, Mach-Zehnderův interferometr

Acknowledgement

I would like to thank Mgr. Michal Mičuda, Ph.D. I appreciate his guidance and driving force. My thanks also goes to Mgr. Miroslav Ježek, Ph.D. for his beneficial consultations and hints. I wish to express my gratitude to other team members that I could cooperate with on this project: Mgr. Ivo Straka, Mgr. Martina Miková, Prof. RNDr. Miloslav Dušek, Dr., Doc. Mgr. Radim Filip, Ph.D. and Doc. Mgr. Jaromír Fiurášek, Ph.D. I also want to thank my family for their kind support and understanding.

Declaration

I declare that I have written this contest contribution “Quantum CZ gate with weak coupling” on my own under the guidance of Mgr. Michal Mičuda, Ph.D. by using theoretical resources, which are referred to in the list of literature. I agree with the further usage of this document according to the requirements of the Department of Optics.

Declared at Olomouc on

Signature

Contents

1	Introduction - CNOT and CZ gates	1
2	Theory	5
2.1	CZ gate	5
2.2	CZ restoration in weak coupling regime	7
3	Implementation of the weak CZ	10
3.1	Principle of operation	10
3.2	Experimental setup	14
4	Experimental characterisation	20
4.1	Stability measurement	20
4.2	Hofmann bound characterisation	26
4.3	Quantum process tomography	30
5	Summary	35
6	Bibliography	37
A	Derivations	i
B	Custom USB voltmeter	viii

1 Introduction - CNOT and CZ gates

As a gentle introduction to the topic, let us first describe classical XOR and control not (CNOT) gate. XOR gate takes two logical inputs and returns logical 1 if and only if inputs do not have equal values, in any other case it returns logical 0. When we copy value from one input of the XOR gate and add it to the output we get the CNOT gate, see Figure 1. The truth table of the classical CNOT gate is given in Table 1.

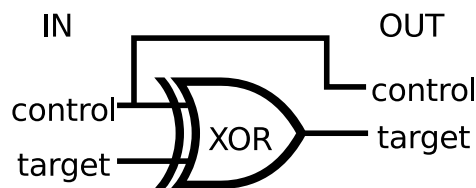


Figure 1: A circuit diagram of the CNOT gate implemented using XOR gate.

input		output	
control	target	control	target
0	0	0	0
0	1	0	1
1	0	1	1
1	1	1	0

Table 1: Classical CNOT truth table. If the control bit is in logical 1, then the output target qubit changes the value. The value of the output target bit is a result of XOR operation on the input target bit and the control bit. The output control bit is a copy of the input control bit.

One can notice that the gate is reversible - applying the gate on the output pair of bits will reproduce the original input. In classical computing, the CNOT gate is not enough to implement arbitrary boolean operation on two bits and it is said, that the CNOT gate is not an universal gate [1]. To achieve classical universal reversible gate, we need to add one more control bit and extend CNOT to CCNOT. This is called the Toffoli gate. However, it is known, that in quantum computing the CNOT together with single-qubit operations is capable of implementing an universal 2-qubit gate [2].

In quantum computing, we use qubits as a quantum analogy to a classical bits. In computation basis we denote logical 1 as $|1\rangle$ state and logical 0 as $|0\rangle$ state, regardless the

actual physical implementation. In quantum mechanics, a superposition of two states is also a state and a qubit can be in arbitrary superposition of both logical states. In Dirac notation we write:

$$|\psi\rangle = \alpha|0\rangle + \beta|1\rangle, \langle\psi|\psi\rangle = 1, \alpha, \beta \in \mathbb{C}.$$

In the analogy to classical CNOT gate we can write desired operation on qubits as:

$$\begin{aligned} |00\rangle &\rightarrow |00\rangle, \\ |01\rangle &\rightarrow |01\rangle, \\ |10\rangle &\rightarrow |11\rangle, \\ |11\rangle &\rightarrow |10\rangle. \end{aligned} \tag{1}$$

One can write the relation also in the matrix form

$$U_{CNOT} := \begin{pmatrix} 1 & 0 & 0 & 0 \\ 0 & 1 & 0 & 0 \\ 0 & 0 & 0 & 1 \\ 0 & 0 & 1 & 0 \end{pmatrix} \tag{2}$$

defining $|0\rangle := \begin{pmatrix} 1 \\ 0 \end{pmatrix}$, $|1\rangle := \begin{pmatrix} 0 \\ 1 \end{pmatrix}$ and $|ab\rangle := |a\rangle \otimes |b\rangle$, where \otimes denotes the Kronecker product. The matrix form suggests that the quantum CNOT gate applies Pauli σ_x operator on the target qubit, if the control qubit is in state the $|1\rangle$. The common symbol for CNOT gate used in circuit diagrams is depicted in Figure 2.

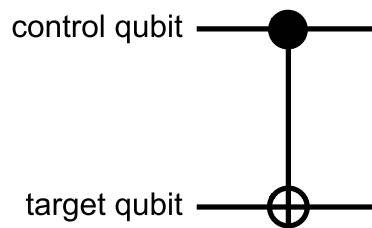


Figure 2: Symbol of a quantum CNOT gate commonly used in quantum circuit diagrams.

The CNOT gate has several interesting properties. Among belonging to set of gates needed to create an universal 2-qubit gate, unitarity and reversibility, it is also maximally entangling. For example, CNOT gate creates maximally entangled state from the separable states:

$$U_{CNOT} \frac{1}{\sqrt{2}}(|00\rangle + |10\rangle) = \frac{1}{\sqrt{2}}(|00\rangle + |11\rangle) = |\Phi^+\rangle.$$

All these interesting properties form the motive of our interest in the CNOT gate.

The quantum control-Z (CZ) gate does not have a classical analogy. CZ gate applies Pauli σ_z operator to the target qubit if the control qubit is in the $|1\rangle$ state. Alternatively we can say that the CZ gate introduces π -phase shift on the target qubit if both control and target qubits are in state $|1\rangle$. We can express CZ operation in similar way as we did for CNOT gate:

$$\begin{aligned} |00\rangle &\rightarrow |00\rangle, \\ |01\rangle &\rightarrow |01\rangle, \\ |10\rangle &\rightarrow |10\rangle, \\ |11\rangle &\rightarrow -|11\rangle, \end{aligned} \tag{3}$$

or in the matrix form

$$U_{CZ} := \begin{pmatrix} 1 & 0 & 0 & 0 \\ 0 & 1 & 0 & 0 \\ 0 & 0 & 1 & 0 \\ 0 & 0 & 0 & -1 \end{pmatrix}. \tag{4}$$

The circuit diagram of CZ gate is shown in Figure 3.

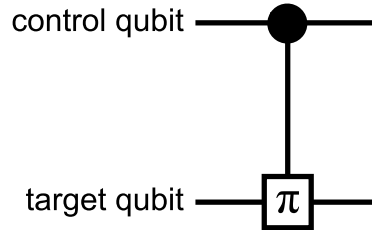


Figure 3: Symbol of a quantum CZ gate we used in quantum circuit diagrams.

CZ and CNOT gates are closely related. To show the relation, we need to introduce $|\pm\rangle$ states generated by the Hadamard operation U_H applied on $|0\rangle$ and $|1\rangle$ states.

$$\begin{aligned} |0\rangle &\rightarrow \frac{1}{\sqrt{2}}(|0\rangle + |1\rangle) := |+\rangle, \\ |1\rangle &\rightarrow \frac{1}{\sqrt{2}}(|0\rangle - |1\rangle) := |-\rangle. \end{aligned} \tag{5}$$

The Hadamard operation could be written also in matrix form

$$U_H := \frac{1}{\sqrt{2}} \begin{pmatrix} 1 & 1 \\ 1 & -1 \end{pmatrix}. \tag{6}$$

Now, think of applying Hadamard transform on input and output of the CZ gate, as shown

in Figure 4. One can easily prove the identity

$$(\mathbb{I} \otimes U_H)U_{CZ}(\mathbb{I} \otimes U_H) = U_{CNOT} \quad (7)$$

which shows that the CNOT gate is equivalent to CZ gate up to the Hadamard transform. Although the topic of this thesis is the CZ gate the motivation mentioned in description of the CNOT gate remains valid due to the equivalence (7) between CNOT and CZ gates.

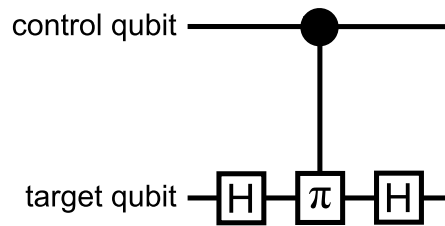


Figure 4: The CNOT gate implemented using the CZ gate and Hadamard gates. Hadamard gates are denoted by boxes with H inside.

Quantum gates are implemented on many physical systems, such as photons [3, 4, 5], trapped ions [6], atomic ensembles [7] or nuclear spins [8]. To implement the quantum gate that operates on more than one qubit, one or more inter-qubit interactions are required. Sometimes the interaction is not strong enough and to provide right interaction between qubits and the quantum gate gets difficult to realize. The motivation of this thesis is to overcome this hurdle and increase the interaction strength.

2 Theory

2.1 CZ gate

Here we describe the linear optical CZ gate into more detail in order to show the principle of its operation. The underlying principle of quantum operation in linear optics is coincidence measurement and quantum interference on a beam splitter [9]. Figure 5 shows the possible implementation of the CZ gate. The control qubit A is encoded into spatial modes A0 and A1. The target qubit B is encoded into spatial modes B0 and B1. One can assign computational states to creation operators:

$$\begin{aligned} |0\rangle_a &:= a_0^\dagger |\text{vac}\rangle, & |1\rangle_a &:= a_1^\dagger |\text{vac}\rangle, \\ |0\rangle_b &:= b_0^\dagger |\text{vac}\rangle, & |1\rangle_b &:= b_1^\dagger |\text{vac}\rangle. \end{aligned} \quad (8)$$

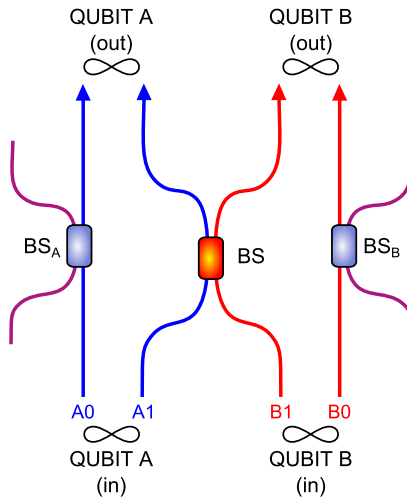


Figure 5: Concept of the CZ gate implemented on linear optics platform. Qubits are encoded into spatial modes: A0, A1 - target qubit A; B0, B1 - control qubit B. BS_A and BS_B as well as BS are beam splitters.

The interaction between modes A1 and B1 is described by the Hamiltonian

$$H_{int} = i\hbar g(a^\dagger b - ab^\dagger), \quad (9)$$

where g is the coupling constant. The Heisenberg equation together with initial condition $a_1(0) = a_{10}, b_1(0) = b_{10}$ yields:

$$\begin{pmatrix} a(t) \\ b(t) \end{pmatrix} = \begin{pmatrix} \cos(g\tau) & \sin(g\tau) \\ -\sin(g\tau) & \cos(g\tau) \end{pmatrix} \begin{pmatrix} a_1(0) \\ b_1(0) \end{pmatrix}. \quad (10)$$

We define amplitude transmittance $t := \cos(g\tau)$ and reflectance $r := \sin(g\tau)$ to obtain the well-known matrix of the beam splitter. We mention this to show the link between strength of interaction between photons and the beam splitter parameters. Transformation relation for a^\dagger and b^\dagger are obtained by Hermitian conjugation.

Beam splitters BS_A and BS_B serve as attenuations of mode A0 and B0, respectively. The central beam splitter provides the interaction between modes A1 and B1 and thus between two qubits. The whole concept operates in coincidence measurement - we accept the outcome only if both output detectors at qubit A and qubit B are triggered simultaneously.

To explain the principle of this CZ gate implementation we discuss four input computation base states. For input $|00\rangle$ both modes A0 and B0 are attenuated with transmittance t_a and t_b , respectively. The output is same as input up to reduction of the amplitude.

For input $|01\rangle$ one of the mode is attenuated and the other undergoes the splitting on the central BS. The photon from mode B1 can be reflected on BS into the mode A1 with amplitude reflectance r . In this case, the photon would be absent on one of detector at the output. The coincidence measurement would not accept such case. Alternatively, the photon can be transmitted with amplitude transmittance t and in this case the output is again the same as input up to reduction of the amplitude. This holds for input $|11\rangle$ as well.

When the input is $|11\rangle$, the quantum interference takes place. In coincidence measurement the output state is $(t^2 - r^2)a_1^\dagger b_1^\dagger |\text{vac}\rangle$. When $T < R$ with $T := t^2$, $R := r^2$ a π -phase shift is introduced. We call this a *strong coupling regime*. Using equations (8) and (10) one can derive

$$\begin{aligned} |00\rangle &\rightarrow t_a t_b |00\rangle, \\ |01\rangle &\rightarrow t_a t |01\rangle, \\ |10\rangle &\rightarrow t_b t |10\rangle, \\ |11\rangle &\rightarrow (T - R) |11\rangle. \end{aligned} \tag{11}$$

We require same size of output amplitudes in relations (11) and a π -phase shift for the last amplitude. These two conditions are satisfied when $t_a = t_b = t = \sqrt{1/3}$. Then the transformation relations are

$$\begin{aligned} |00\rangle &\rightarrow \frac{1}{3} |00\rangle, \\ |01\rangle &\rightarrow \frac{1}{3} |01\rangle, \\ |10\rangle &\rightarrow \frac{1}{3} |10\rangle, \\ |11\rangle &\rightarrow -\frac{1}{3} |11\rangle, \end{aligned} \tag{12}$$

which are the same as relations (3) up to amplitude reduction. One might see, that the CZ gate works with a limited success probability of $1/9$. Detailed computation of these

relations is in the Appendix A, point (a).

The control-Z gate has already been implemented using linear quantum optics [3, 4, 5]. However, not every platform supports arbitrary choice of t which is related to the strength of qubit interaction. In cases where $T > R$, π phase shift does not occur. We say that the interacting systems are in a *weak coupling regime* and the CZ gate can not be accomplished this way.

2.2 CZ restoration in weak coupling regime

In this section we propose how to overcome the obstacle of weak coupling regime. The proposal is depicted in Figure 6. The central beam splitter has not the suitable transmittance and $T < R$ is not satisfied. In comparison to Figure 5 there is an extra auxiliary bypass mode C which is coupled to mode A1. By means of this coupling, only a fraction of original mode A1 interacts with mode B1. After the interaction, mode C is projected back to mode A1. This counter-intuitively leads to the restoration of the CZ operation.

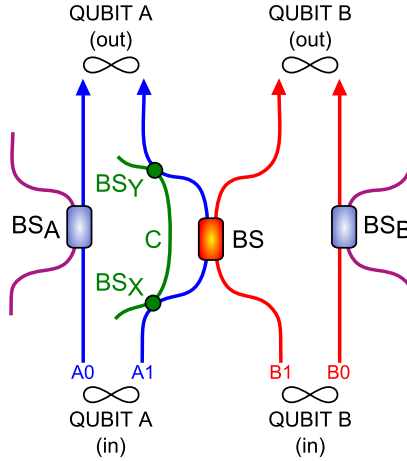


Figure 6: Concept of the CZ gate with weak coupling. The concept was extended by the bypass channel C in contrast to Figure 5. The channel C allows the restoration of CZ operation in weak coupling regime.

Let t_a , t_b and t be transmission coefficient of BS_A , BS_B and BS . Additionally, let t_x and t_y be transmission coefficient of auxiliary beam splitters BS_X and BS_Y . After some

algebra, one obtains transformation relations

$$\begin{aligned}
|00\rangle &\rightarrow t_a t_b |00\rangle, \\
|01\rangle &\rightarrow t_a t |01\rangle, \\
|10\rangle &\rightarrow t_b (t t_x t_y + r_x r_y) |10\rangle, \\
|11\rangle &\rightarrow [t_x t_y (2t^2 - 1) + r_x r_y t] |11\rangle.
\end{aligned} \tag{13}$$

For more details about derivation see Appendix A, point (b). From conditions on the same output amplitude sizes and π -phase shift we obtain

$$\begin{aligned}
t_b &= t, \\
t_a &= t t_x t_y + r_x r_y, \\
\frac{t_x t_y}{r_x r_y} &= \frac{2t}{1-3t^2}.
\end{aligned} \tag{14}$$

Success probability of the CZ operation is

$$P_S := \frac{1}{4} \sum_{i,j=0}^1 |\langle ij | U_{wCZ} | ij \rangle|^2. \tag{15}$$

Since sizes of all output amplitudes are the same, one obtains

$$P_S = \frac{1}{4} t_x^2 t_y^2 R^2 \tag{16}$$

which is maximized when

$$t_x^2 = t_y^2 = \frac{2t}{2t + |1 - 3t^2|}, \tag{17}$$

as discussed in Appendix (A), point (c).

The process matrix (Choi matrix) χ is a standard tool to describe a quantum process. To compute the process matrix that corresponds to the unitary matrix U we introduce the entangled state

$$|\Phi\rangle := \frac{1}{2} (|00\rangle|00\rangle + |01\rangle|01\rangle + |10\rangle|10\rangle + |11\rangle|11\rangle), \tag{18}$$

where one subsystem corresponds to the input qubit space and the other to the output qubit space. The process matrix is

$$\chi := (\mathbb{I} \otimes U) |\Phi\rangle \langle \Phi| (\mathbb{I} \otimes U)^\dagger. \tag{19}$$

To demonstrate the CZ restoration, we assume central beam splitter with $t = \sqrt{\frac{2}{3}}$. In the first step we do not use bypass, $t_x = 1$. Then also according to conditions (14) we have $t_a = t_b = t$ and the third condition of (14) is not satisfied. The process matrix is visualized in Figure 7 (a). One can see that the process matrix looks like an identity operation up to mode-selective attenuation. If we use arbitrary bypass strength $t_x \neq 0$ and with t_a, t_b and t_y satisfy conditions (14), then we obtain the process matrix identical to the ideal process matrix of the CZ gate, see Figure 7 (b).

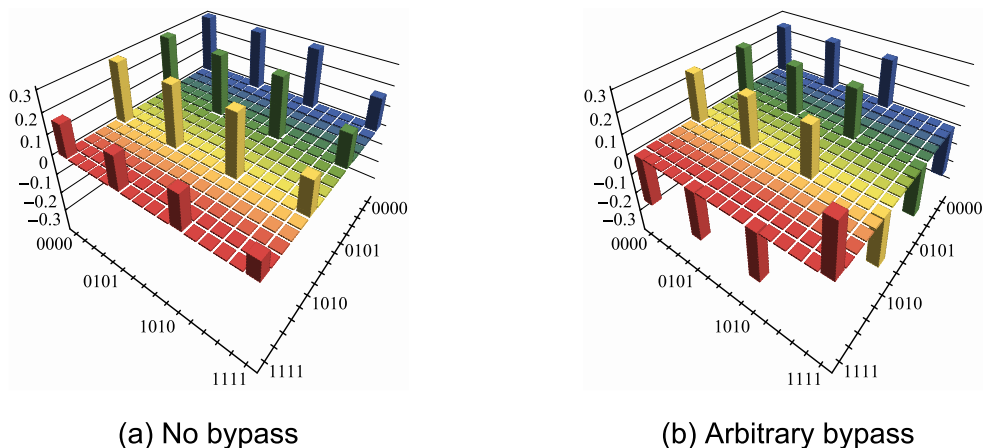


Figure 7: The CZ gate operation in the weak coupling regime. (a) No bypass - the process matrix resembles the identity matrix, but is far from CZ matrix. (b) Arbitrary bypass - conditions (14) are satisfied and the process matrix is identical to the process matrix of the ideal CZ gate. Only real parts of the process matrices are plotted, because imaginary parts are identically zero.

We define the process fidelity [10]

$$F_{\chi_1, \chi_2} = \frac{\text{Tr}[\chi_1 \chi_2]}{\text{Tr}[\chi_1] \text{Tr}[\chi_2]} \quad (20)$$

in order to quantify the overlap between two process matrices. The fidelity of the process matrix with bypass with respect to the ideal CZ process matrix is indeed $F_\chi = 1$. The success probability is a function of bypass coupling strength and is generally lower than the success probability of the ideal CZ gate. The dependence of the success probability on the bypass coupling strength is discussed in Section 4.2.

3 Implementation of the weak CZ

3.1 Principle of operation

Our implementation utilizes a photon pair generator, bulk linear optics, polarization and spatial encoding and a coincidence post selection. Here we describe the working principle of the implemented CZ gate in analogy to the scheme depicted in Figure 6. To show the analogy graphically, the CZ gate implementation is presented in Figure 8. Block-wise explanation of the analogy follows.

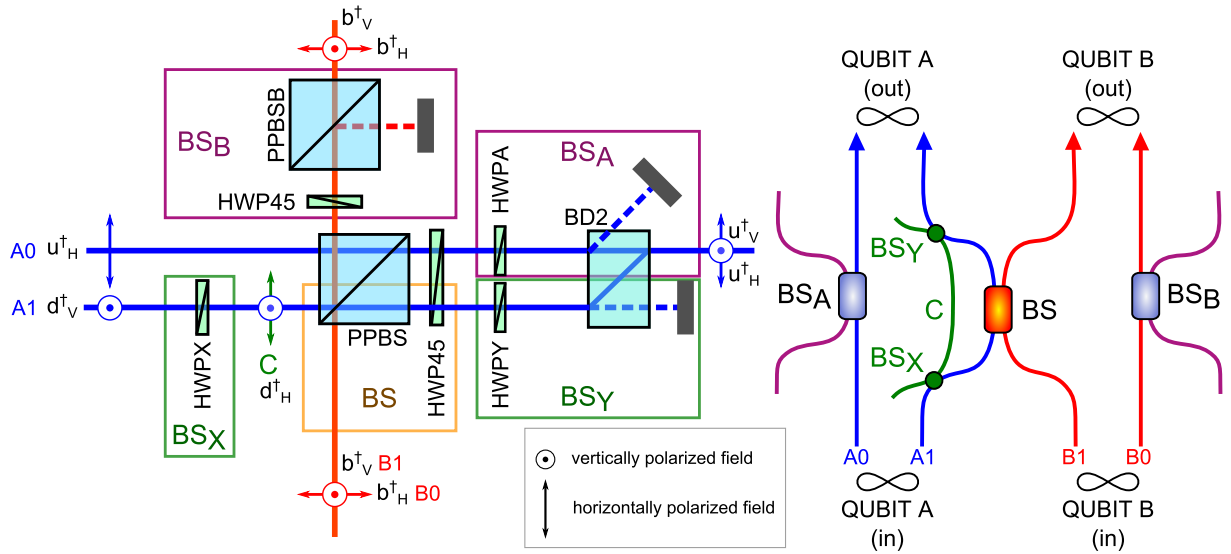


Figure 8: Analogy of our implementation of CZ gate (left) to the proposed scheme (right). Blue paths belong to control qubit, red paths to target qubit. Auxiliary bypass mode is denoted by green colour. Violet regions represent implementation of attenuators BS_A and BS_B . Green areas take role of $BS_{X,Y}$. Orange area represents the central BS where two-photon interference occurs. HWP - half-wave plate, PPBS - partially polarizing beam-splitter, BD - beam displacer. Dark grey boxes represent beam stops.

To understand the operation principle, it is important to define the qubit encoding. The control qubit A is encoded into spatial modes of the Mach-Zehnder (MZ) interferometer. We assign spatial modes to computation basis states $|0\rangle_c = u_H^\dagger|\text{vac}\rangle$, $|1\rangle_c = d_V^\dagger|\text{vac}\rangle$. Only a part of the interferometer is depicted, because the first part of the interferometer is not used in gate itself, but it belongs to a preparation stage. The preparation stage is described in the next section. The input target qubit B is encoded into polarization modes, formally written $|0\rangle_t = b_H^\dagger|\text{vac}\rangle$, $|1\rangle_t = b_V^\dagger|\text{vac}\rangle$. The output control qubit is encoded into polarization modes $|0\rangle_c = u_V^\dagger|\text{vac}\rangle$, $|1\rangle_c = u_H^\dagger|\text{vac}\rangle$ and the output target qubit is encoded into polarization modes $|0\rangle_t = b_V^\dagger|\text{vac}\rangle$, $|1\rangle_t = b_H^\dagger|\text{vac}\rangle$.

The core of the gate is the partially polarizing beam splitter (PPBS) which ideally reflects only vertically polarized component and thus provides Hong-Ou-Mandel (HOM) interference only between mode d_V (analogy to A1) and b_V (analogy to B1). HWPX couples d_V to d_H (analogy to C) which creates the bypass channel. The coupling is described by transformation

$$\begin{aligned} d_H &\rightarrow -\cos(2\phi_x)d_H + \sin(2\phi_x)d_V, \\ d_V &\rightarrow \cos(2\phi_x)d_V + \sin(2\phi_x)d_H. \end{aligned} \quad (21)$$

Therefore we can assign amplitude transmission of BS_X to angle of HWPX, $t_x := \cos(2\phi_x)$. In order to achieve correct signal collection after the BD2, we swap vertically and horizontally polarized components using HWP rotated to 45 degrees. HWPY together with BD2 projects bypass mode b_V (b_H before swapping) to b_H (now analogous to A1). The transformation is

$$\begin{aligned} d_H &\xrightarrow{\text{HWPY, BD2}} \cos(2\phi_y)d_H, \\ d_V &\xrightarrow{\text{HWPY, BD2}} \sin(2\phi_y)d_H. \end{aligned} \quad (22)$$

HWP rotated to 45 degrees together with PPBSB provides attenuation of mode b_H , similarly as BS_B . HWPA together with BD2 provides attenuation of mode u_v and takes the role of BS_A .

The actual implementation suffers from parasitic reflectance R_H at PPBS and partial distinguishability of idler and signal photons. In our theoretical model, we take these imperfections into account. For case of indistinguishable photons we obtain the input-output relation U_{wCZ}

$$\begin{aligned} |00\rangle &\rightarrow [t_a t_H^2 t] |00\rangle, \\ |01\rangle &\rightarrow [t_a t_H^2 t] |01\rangle, \\ |10\rangle &\rightarrow [t_x t_y t_H t^2 + r_x r_y (t_H^2 - r_H^2)] |10\rangle - [t_x r_y t_H r_H r] |11\rangle, \\ |11\rangle &\rightarrow [t_x t_y (t^2 - r^2) + r_x r_y t_H^2 t] |11\rangle - [t_y r_x r_H t r] |10\rangle, \end{aligned} \quad (23)$$

where $t_{x,y} := \cos(2\phi_{x,y})$, $r_{x,y} := \sin(2\phi_{x,y})$, $t = t_b$, $t_a := \cos(2\phi_a)$ and t_h, r_h are amplitude transmittance and reflectance of the central PPBS for horizontally polarized component.

We model imperfect HOM interference as a mixture of perfectly indistinguishable photons with probability q and perfectly distinguishable photons with probability $(1 - q)$. We use the following definition of HOM visibility:

$$\nu := \frac{C_{\max} - C_{\min}}{C_{\max} + C_{\min}}, \quad (24)$$

where C_{\min} denotes the coincidence count rate in the HOM dip and C_{\max} denotes the

coincidence count rate far away from the dip, where photons are distinguishable. Then the probability q is related to HOM dip visibility ν by equation

$$q = \frac{2\nu}{1 + \nu}. \quad (25)$$

Assume four possible scenarios for two perfectly distinguishable photons A and B. Photon A is reflected and photon B is transmitted, B is reflected and A is transmitted, both are transmitted or both are reflected. First two cases would not trigger the coincidence, because there are two photons on one output and no photon on the other one. In latter two cases we get the unwanted operation. In the case where both photons are transmitted, the transformation O_{tt} is

$$\begin{aligned} |00\rangle &\rightarrow t_a t_H^2 t |00\rangle, \\ |01\rangle &\rightarrow t_a t_H^2 t |01\rangle, \\ |10\rangle &\rightarrow t_h t (t_x t_y t + r_x r_y t_H) |10\rangle, \\ |11\rangle &\rightarrow t_h t (t_x t_y t + r_x r_y t_H) |11\rangle. \end{aligned} \quad (26)$$

Similarly for case, where both photons are reflected, the transformation O_{rr} is

$$\begin{aligned} |00\rangle &\rightarrow 0, \\ |01\rangle &\rightarrow 0, \\ |10\rangle &\rightarrow -r_H^2 r_x r_y t |10\rangle - r_H t_x r_y r t_H |11\rangle, \\ |11\rangle &\rightarrow -r^2 t_x t_y t_H |11\rangle - r r_x r_h t_y t |10\rangle. \end{aligned} \quad (27)$$

Detailed computation of relations (23),(26) and (27) can be found in Appendix A, point (d).

To obtain the overall process matrix we can add process matrix of indistinguishable photons case weighted by factor q and process matrices of distinguishable photons weighted by factor $(1 - q)$. The overall process matrix is

$$\begin{aligned} \chi = & q(\mathbb{I} \otimes U_{wCZ})|\Phi\rangle\langle\Phi|(\mathbb{I} \otimes U_{wCZ})^\dagger + \\ & (1 - q)[(\mathbb{I} \otimes O_{rr})|\Phi\rangle\langle\Phi|(\mathbb{I} \otimes O_{rr})^\dagger + (\mathbb{I} \otimes O_{tt})|\Phi\rangle\langle\Phi|(\mathbb{I} \otimes O_{tt})^\dagger]. \end{aligned} \quad (28)$$

Equation (28) provides the theoretical model of our gate. To characterize the vulnerability of the gate to the experimental imperfections $\nu < 1$, $r_H > 0$, we plotted the process fidelity, given by equation (20), as function of r_H , ν . The parameters we use are $R = 0.313$ and $\phi_x = 20.0^\circ$. The graph is shown in Figure 9.

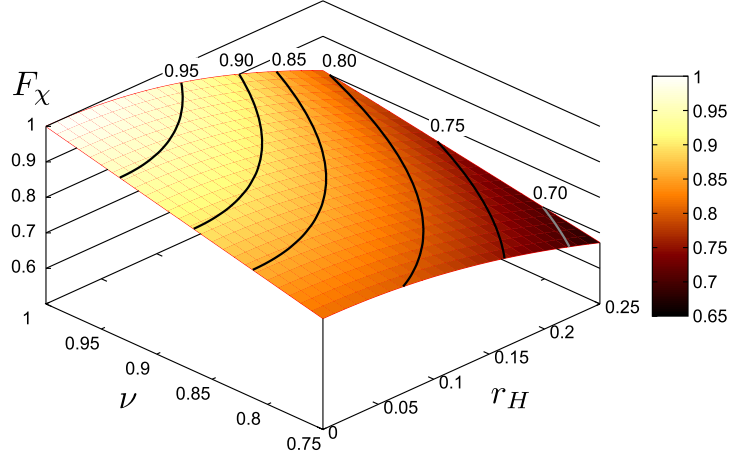


Figure 9: Vulnerability of the CZ gate fidelity to imperfections of the implementation - parasitic reflectance r_H and HOM dip visibility ν . The surface is shaded in false colours that are related to the process fidelity value by presented colour bar. For realistic parameters of the model $r_H = 0.137$, $\nu = 0.94$, the process fidelity is $F_\chi = 0.898$.

The contour lines in the figure give information about steepness of the fidelity function and thus about the vulnerability to experimental imperfections. At first, the fidelity is more tolerant to parameter r_H than ν . But then the r_H becomes more important and the the decrease of the fidelity is faster. For parameters $r_H = 0.137$, $\nu = 0.94$, $R = 0.313$ and $\phi_x = 20.0^\circ$ we plotted also the process matrix, see Figure 10 (a). Comparing to the ideal CZ process matrix in Figure 10 (b), one can observe extra non-zero elements and disturbance of originally equal amplitude sizes.

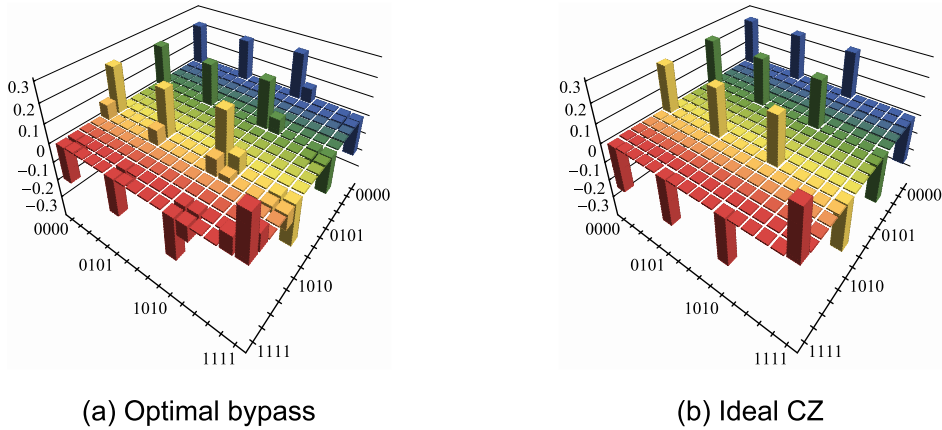


Figure 10: (a) The process matrix of our implementation $r_h = 0.137$ and $\nu = 0.94$. Only real part is plotted because the imaginary part is identically zero. Phase shifts were not taken into account. (b) Ideal CZ process matrix.

3.2 Experimental setup

The experimental setup is depicted in Figure 11. Time-correlated photon pairs are generated by the process of collinear frequency-degenerate type-II spontaneous parametric down-conversion in a 2 mm thick BBO crystal pumped by a 100 mW continuous-wave laser diode at 405 nm wavelength.

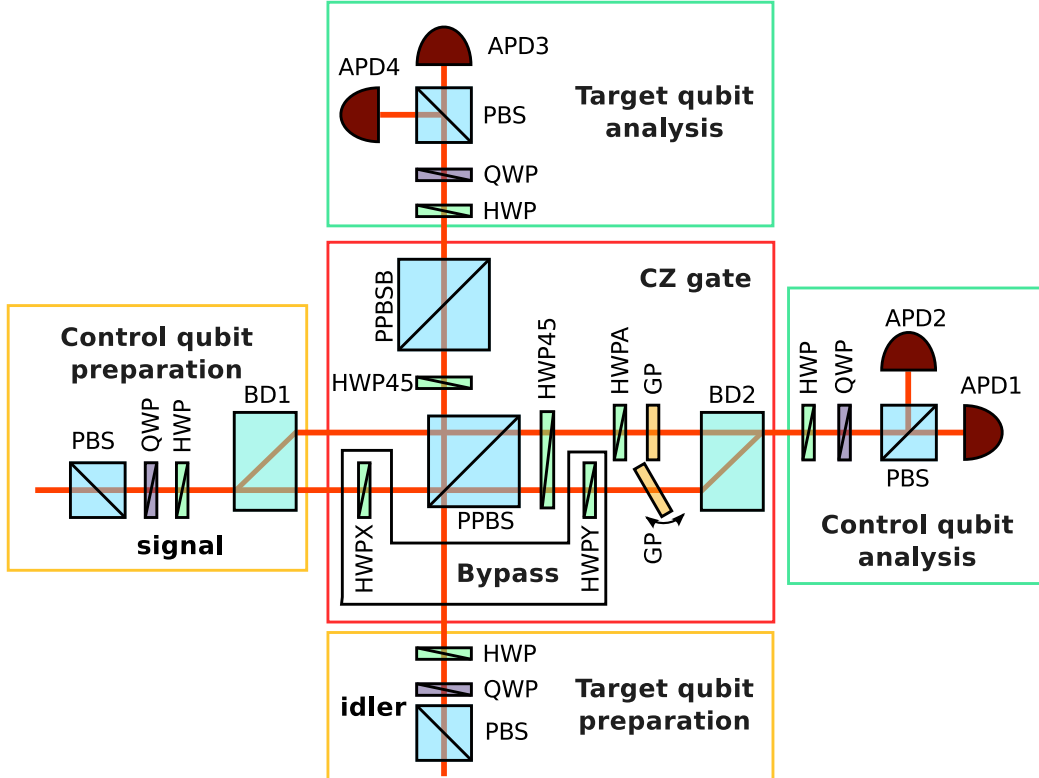


Figure 11: Experimental setup. PBS - polarizing beam splitter, HWP - half-wave plate, QWP - quarter-wave plate, BD - calcite beam displacer (horizontally polarized component is displaced), PPBS - partially polarizing beam splitter, GP - glass plate, APD - avalanche photodiode detector.

Signal and idler photons are brought from the pair generator via single mode optical fibres and polarization controllers into the preparation stages. The control qubit is encoded into spatial modes of the MZ interferometer - the top arm for the $|0\rangle$ state and the bottom arm for the $|1\rangle$ state. The spatial encoding is implemented by manipulating polarization state of the signal photon and then introducing spatial transversal offset on the calcite polarizing beam displacer BD1. The actual polarization state manipulation is implemented by quarter-wave (QWP) and half-wave (HWP) plates. Horizontally polarized component

is spatially displaced by approximately 4 mm with respect to vertically polarized component. The small distance between the arms of the MZ interferometer improves the phase stability of the MZ interferometer but requires modified optical elements - details are in Figure 12. The target qubit is encoded into polarization modes - horizontally polarized mode for logical $|0\rangle$ and vertically polarized mode for logical $|1\rangle$.

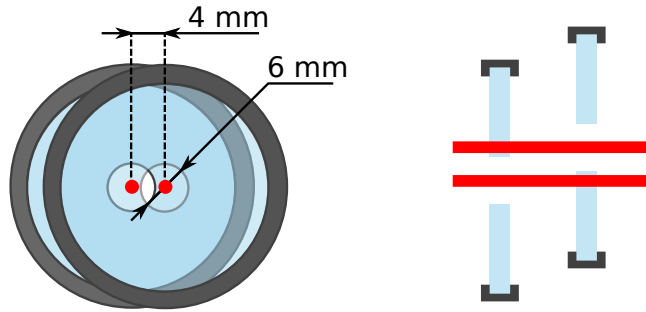


Figure 12: Wave plate modification for the interferometer arm - front and top view. There is need for controlling polarization state in both arms of the interferometer. Thanks to the opening in the centre of the wave plate, one arm of the interferometer is not influenced. A pair of wave-plates, placed as shown in the picture, provide the polarization control of both arms independently. Arms of the interferometer are denoted by red colour. These waveplates were manufactured by Toptec Turnov.

The gate itself works as described in Section 3.1. In comparison to Figure 8, beam stops are not present because the optical signal is either blocked by components aperture or is simply not collected. The amplitude reflectance of the central PPBS for vertically polarized mode is $R = 0.559^2 = 0.313$. The parasitic reflectance is $R_H = 0.137^2 = 0.019$. Spatial and time overlap of the signal photon and the idler photon on the PPBS is important because it is connected to distinguishability of the photons. Coupling into single mode optical fibres in detection blocks provides spatial filtering which improves the spatial overlap. The time overlap is adjusted using free space delay line in the source of photon pairs. The achieved HOM visibility is $\nu = 0.94$ which yields $q = 0.97$ probability of indistinguishable photons in pair.

Glass plates (GP) are placed into both arms to control the relative phase between arms of the MZ interferometer. We are changing optical path difference between the arms of the MZ interferometer by tilting of the GP. This change in optical path difference results in the phase shift.

HWP, QWP and the polarizing beam splitter (PBS) in the detection block provide projection to arbitrary polarization state. The photons are coupled via collimator into the single-mode optical fibre, where spatial filtering occurs. Detection is provided by the avalanche photodiodes (APD). The signal from the APD is processed electronically to measure in coincidence basis - the reader can find more details in Figure 13. All relevant coincidences - APD1&APD3, APD1&APD4, APD2&APD3 and APD2&APD4 are taken to have information about complementary projections. To avoid the calibration of APD detection efficiencies, we used only coincidences between APD2&APD3 for further analysis.

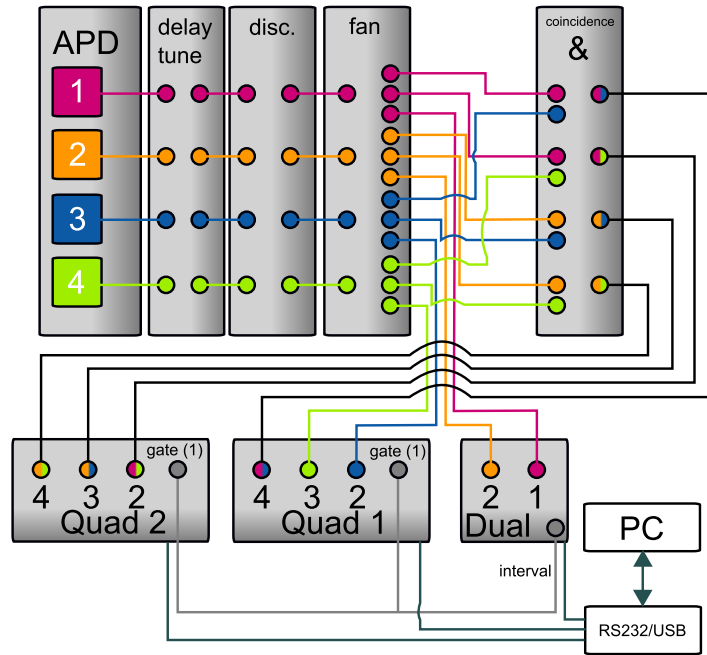


Figure 13: Coincidence detection - electronics part. TTL pulses from the APD modules are converted to NIM-standard pulses and brought through the tunable delay lines to the discriminator (disc.), where the coincidence window 2.6 ns is set. The output signal of each discriminator is split by fan-out module. The outputs from the fan-out module are connected directly to counter electronics as well as coincidence modules. There the AND operation between channels is performed and the output is fed to the counter electronics. The counter electronics is controlled via RS232 bus by the computer. This setup gives us access to all single counts from the APD modules and coincidences between APD1&APD3, APD1&APD4, APD2&APD3 and APD2&APD4.

Before every measurement, a maintenance procedure is done. Thermal fluctuations and mechanical vibration in the laboratory caused slight decrease of optical fibre coupling efficiency and change of the phase in the MZ interferometer. Also a position of HOM dip might change very slightly.

First step of the maintenance procedure is to adjust the spatial overlap of the signal and the idler photons on the central PPBS. The idler input is blocked and the signal input is prepared in the $|1\rangle_c$ state which represents vertically polarized photons in the bottom arm of the MZ interferometer. At the PPBS the signal is split and propagates to both outputs analysis blocks. HWPX and HWPY are set to be zero so they do not modify the polarization of the vertically polarized light. They stay in this position through the whole maintenance procedure. We set the control qubit analysis to project photons into horizontally polarized state and therefore to APD1 detector. By changing tip and tilt of the coupling device we maximize singles count rate on detector APD1. Similarly we maximize the count rate on remaining detectors APD2, APD3 and APD4. At this point the optical path of the signal photon is well spatially defined. Then we adjust the optical path of the idler photon to match the optical path of signal photon and have a good spatial overlap on the PPBS. We block signal photons and allow the idler photons to enter the setup. At the target qubit preparation stage we set the input idler qubit polarization to vertical, which is denoted as $|1\rangle_t$ in the computational basis. The control qubit analyser projects to horizontally polarized states. By changing tip and tilt of the idler decoupling collimator we achieve the maximal singles count rate on detector APD1. The optical paths of both photons are matched and the spatial overlap of signal and idler photons is maximized on PPBS.

The next step is to achieve a good time overlap of the signal and the idler photons. The signal photons are again prepared in the $|1\rangle_c$ state and the idler photons are prepared in vertically polarized state. By changing the length of the delay line in the photon pair source and recording coincidence count rate between detectors APD1 and APD3 we scan the HOM dip. We set the delay line to be in the dip and time overlap of photons is achieved.

The last step is to set the phase of the MZ interferometer. The idler input is blocked and the control qubit preparation stage prepares signal photons in diagonally polarized state which results in balanced superposition of top and bottom mode of the MZ interferometer. At the control qubit detection block we project to the diagonally polarized state as well. By tilting the GP we are trying to find minimal count rate on detector APD2. At this point the phase is set, we unblock the idler input and maintenance procedure ends.

Because the full tomography measurement of the gate requires 1296 measurements, there is need for automation of the measurement. The wave plates in the qubit preparation and the qubit detection blocks are mounted in the motorized mounts, as well as HWPX, HWPY and HWP in the interferometer. The mounts and the counter modules are remotely controlled via RS232 interface by the computer. We employ a Python script

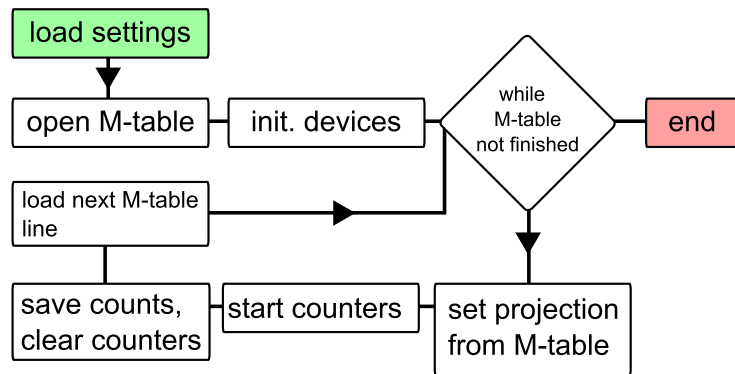


Figure 14: Main procedure (core.py). The M-table, file with projection and setup settings (wave plates angles), is opened and parsed to be processed. The script initializes connected devices. Then it goes through the M-table, controls wave-plates angles, counter modules and saves the data.

to control the experiment.

The script loads the table of the wanted measurements (referred as “M-table” in our schematics) and then performs them. Details about the main script procedure are in Figure 14. In order to make the code more comprehensible, extensible and reusable, the approach of the simple main script with appended custom modules is chosen. These modules are mainly facilitating serial communication with the hardware. The script structure is illustrated in Figure 15.

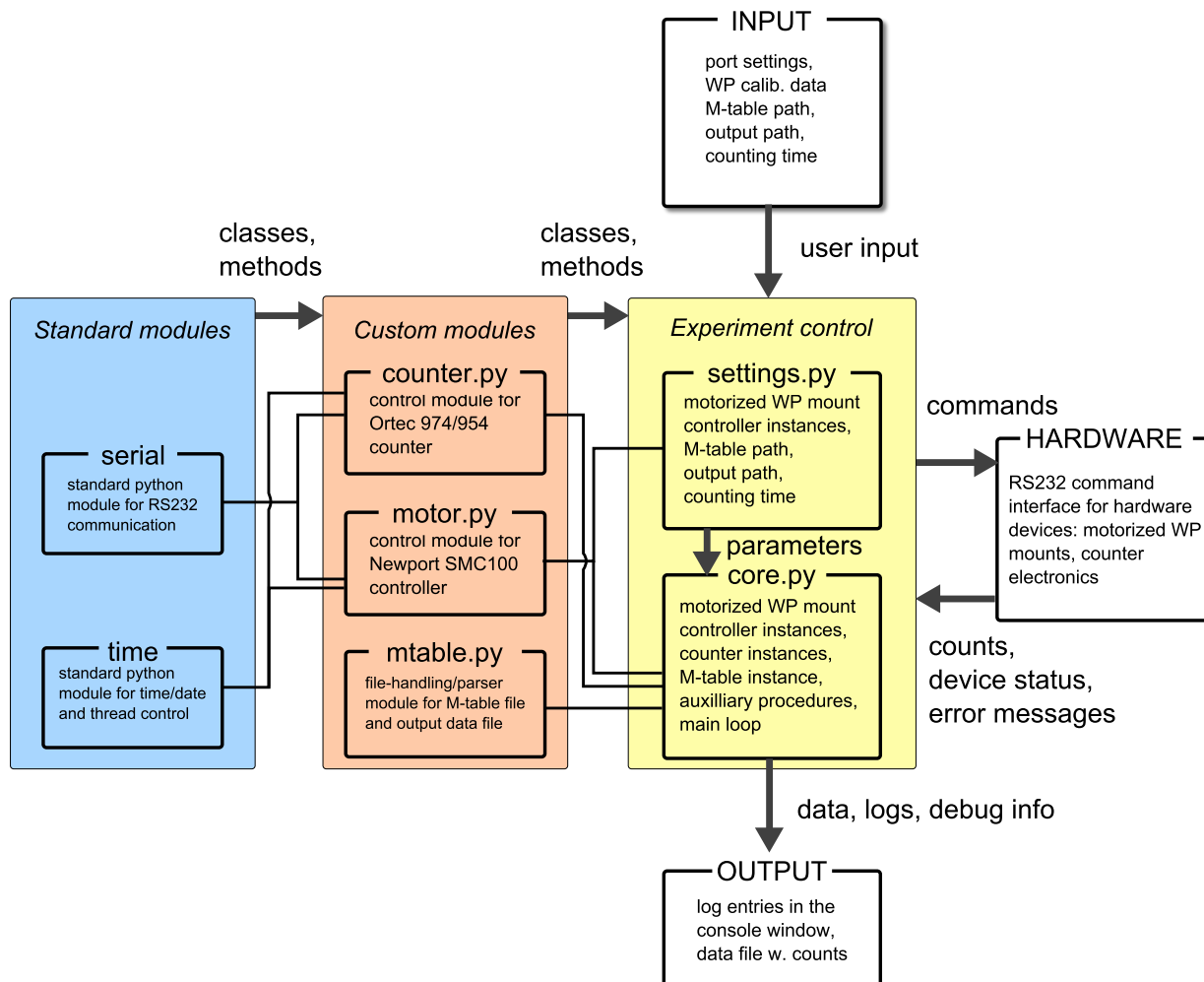


Figure 15: Script structure. The experiment control layer is build upon a custom module layer. The purpose of modules `motor.py` and `counter.py` is to encapsulate serial communication with connected devices into a convenient objects that can be easily used in other scripts. The custom module layer can be extended in order to add more types of devices to the experiment. The custom module layer provides classes and methods to the experiment control layer. The input for the program is provided by means of M-table and `settings.py` file, where serial ports to devices and other things are set. These parameters are handed to the `core.py` script which provides the main procedure described in Figure 14. The script sends commands to devices and gets feedback (with help of custom modules) from them. The data are saved in the output file. The current measurement status is also printed into the console window.

4 Experimental characterisation

4.1 Stability measurement

The phase between the arms in the MZ can affect the gate output, therefore the phase stability is an important parameter of the experimental setup and has to be characterized. The experimental setup for the phase stability characterisation is depicted in Figure 16.

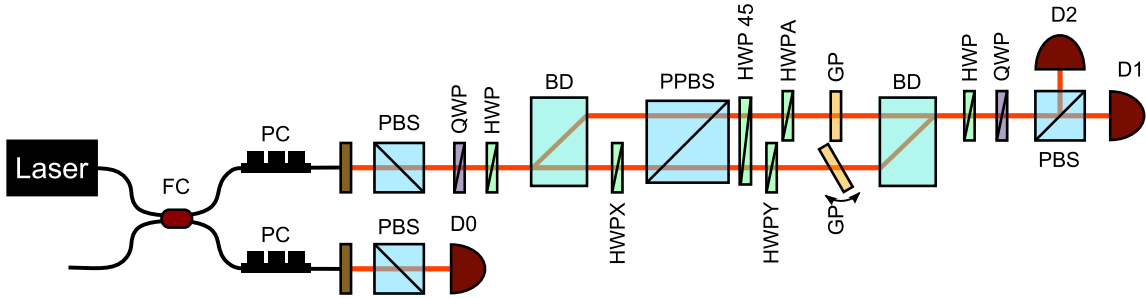


Figure 16: Phase stability characterisation setup: FC - fibre coupler, PC - polarization controller, PBS - polarizing beam splitter, BD - calcite beam displacer, PPBS - partially polarizing beam splitter, HWP - half-wave plate, QWP - quarter-wave plate, GP - glass plate, D0, D1 and D2 - PIN diodes.

We use the temperature stabilized laser diode with central wavelength at 810 nm and spectral full width at half maximum 1.8 nm as a source instead of the photon pair generator. The coherence length is estimated to be $160 \mu\text{m}$. The laser diode is coupled into a single mode optical fibre and guided via fibre coupler (FC) and polarization controller (PC) into the setup. The second output from the FC is guided to reference detection part.

The $|+\rangle$ state is prepared in control qubit preparation stage. The $|+\rangle$ state represents equal superposition of photons in top and bottom arm of the MZ interferometer. Glass plates can be tilted to change the phase within the MZ interferometer. HWPX, HWPY and HWPA are set to 0 degrees, where they don't modify horizontally and vertically polarized states. The output from the MZ interferometer is projected onto $|+\rangle$ and $|-\rangle$ states using the control qubit detection block. The phase fluctuation within MZ interferometer results in intensity fluctuations of projections, which we measure by PIN diodes D1, D2. In order to discriminate between phase fluctuations and laser diode fluctuations there is also a reference channel D0. To avoid confusion, note that we don't use coincidence measurement. Before the data acquisition, we set the phase the same way as we do in the maintenance procedure described in previous section.

A logger of our own construction is used to acquire the data. The motivation and technical details are discussed in the Appendix B. The logger provides 17 bit resolution within range of 0 - 2048 mV. Acquisition sampling rate is set to 0.5 SPS.

The achieved interference visibility of the MZ is $V = 0.988$ in fibre. The log contains 87 hours of data. Even in the raw data, see Figure 17, one can observe that phase deviation is quasi-periodic in several areas. Closer look on the data shows that the laser diode fluctuates approximately with same frequency as intensity fluctuations on detector D1 and detector D2. The laser fluctuations affect signal from detectors D1 and D2 less than the phase fluctuations. The laser intensity is fluctuating slow enough to be sampled by the logger. This observation justifies the use of data normalization to the reference channel.

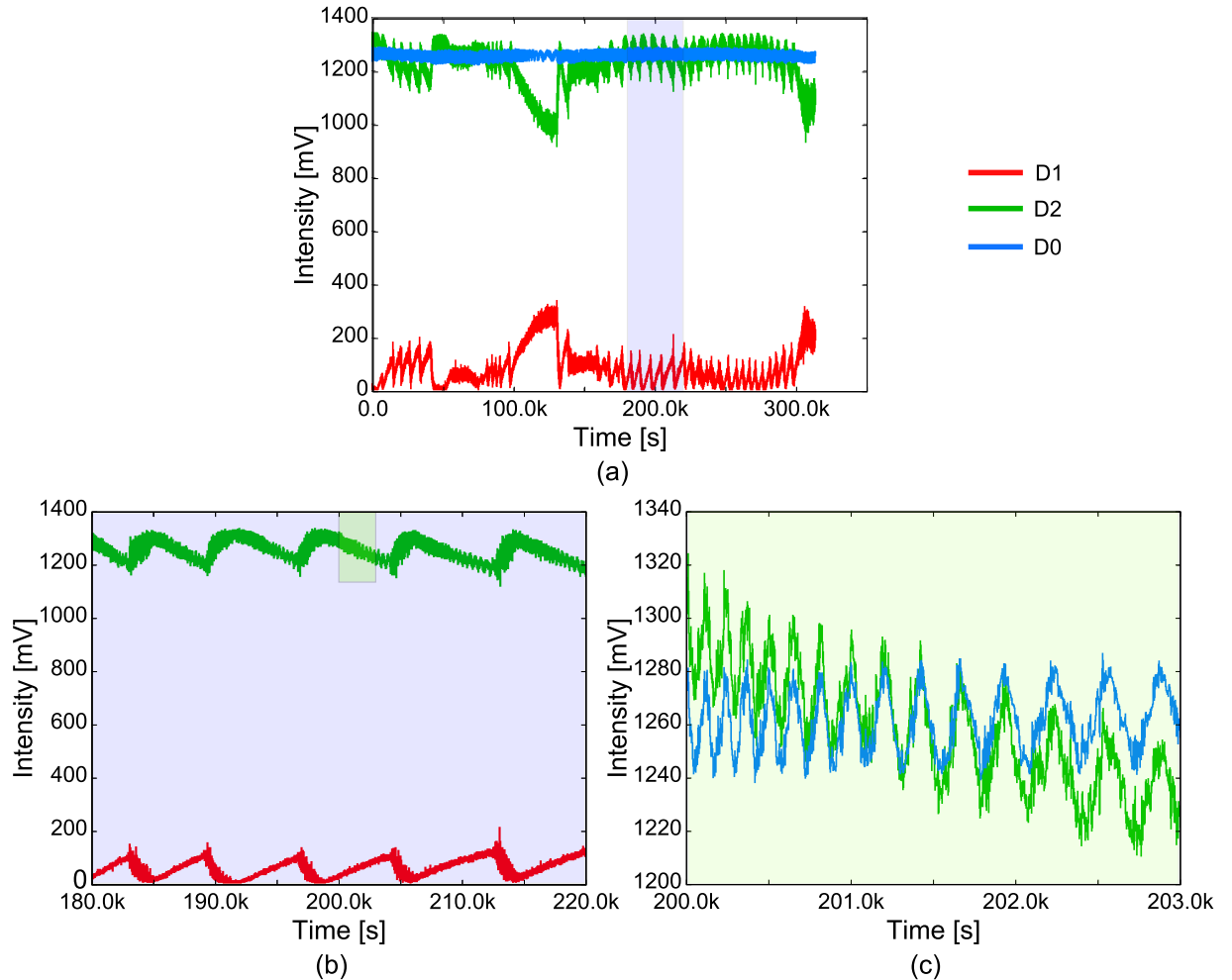


Figure 17: (a), (b), (c): Raw data. D1, D2 and D0 signals are represented as red, green and blue lines. Multiple levels of zoom are used. Part (a) shows the overall data, part (b) highlights the quasi-periodicity of phase fluctuations and part (c) shows the fluctuation of the laser diode.

We use reference signal from detector D0 to normalize signals from detectors D1 and D2 in order to compensate for laser diode intensity fluctuations. The compensated intensity is

$$\tilde{I}_i = \frac{I_i I_{0,\text{REF}}}{I_{i,\text{REF}}}, \quad (29)$$

where \tilde{I}_i is i -th intensity data point, $I_{i,\text{REF}}$ is the i -th value of the reference intensity. From the interference law we calculate the phase-shift

$$\phi_i = \arccos \left(\frac{I_{\text{max}} + \tilde{I}_{\text{min}} - 2\tilde{I}_i}{I_{\text{max}} - \tilde{I}_{\text{min}}} \right), \quad (30)$$

where I_{max} is the D1 signal at the interference maximum and \tilde{I}_{min} is the minimum of all normalized data points. We do not normalize I_{max} , because it was measured right before the acquisition and therefore ratio $\frac{I_{0,\text{REF}}}{I_{1,\text{REF}}}$ is close to one. The maximal phase deviation (with respect to initial phase) in three and half days in the measured data is 60° .

The phase stability is analysed using the Allan variance method [11]. The phase Allan deviation of integration time τ is

$$A = \sqrt{\frac{1}{2(n-1)} \sum_{i=0}^n [y(\tau)_{i+1} - y(\tau)_i]^2}, \quad (31)$$

where n is the number of time bins of length τ and y_i is the average value of phase shift in the data time bin. The lowest possible τ is given by the sampling rate and the highest possible time is given by the duration of the measurement. $A(\tau)$ calculated from the data is depicted in Figure 18. First the deviation decreases as τ increases, where the $A(\tau)$ reaches minimum, the drift starts to be significant and causes the phase Allan deviation to grow. ‘‘Ripples’’ in curve for longer integration times are probably caused by quasi-periodicity in fluctuations.

The phase Allan deviation measures deviation between two samples of some integrating time rather than the actual phase. Therefore we present the phase histogram calculated from all 87 hours of data, see Figure 19 (a). One can observe that the distribution is not Gaussian probably due to drifts and periodicity in the signal. The most frequent value is not close to zero - the phase drifted away and then fluctuated around the certain point. The histogram in Figure 19 (b) is calculated from first six hours of data. This corresponds to the duration of tomography measurement. With respect to this observation we expect, that the reconstructed process will be biased by the phase.

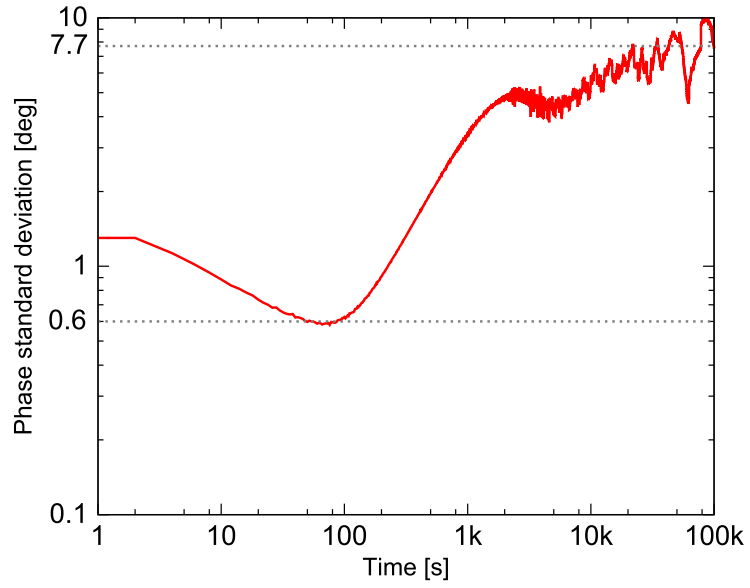


Figure 18: Phase standard deviation dependence on the integration time. The minimum is 0.6° and occurs at integration time 76 s. At the integration time of 6 hours, the standard phase deviation is 7.7° .

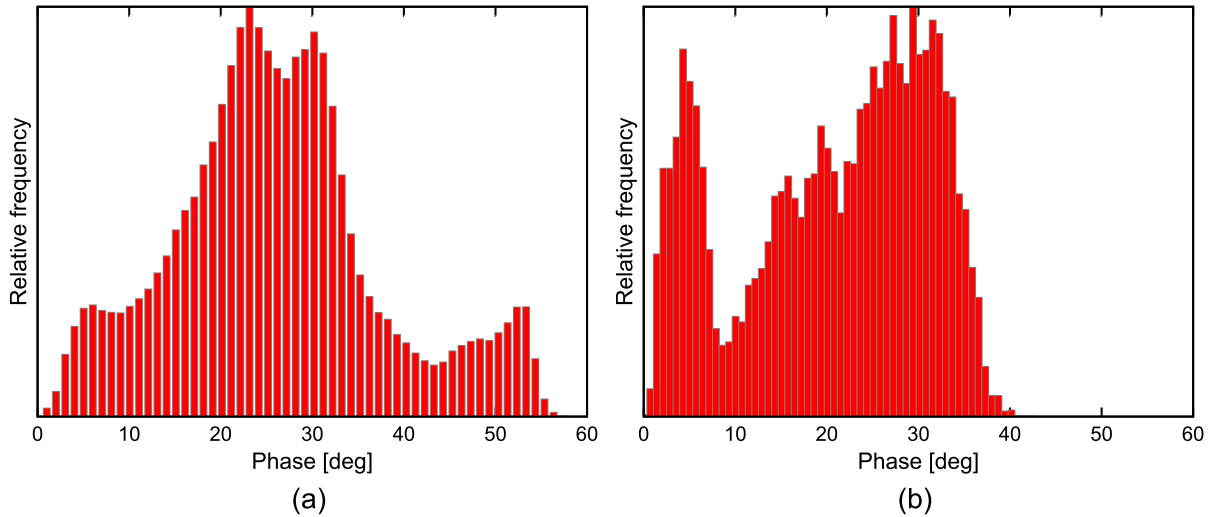


Figure 19: Normalized histograms of the absolute value of the phase. The relative frequency of occurrence versus absolute value of phase is plotted. (a) Complete set of data. (b) Data part of the first 6 hours, which is the typical typical time of the tomography measurement. The mean weighted phase in (b) is $\bar{\phi} = 21^\circ$.

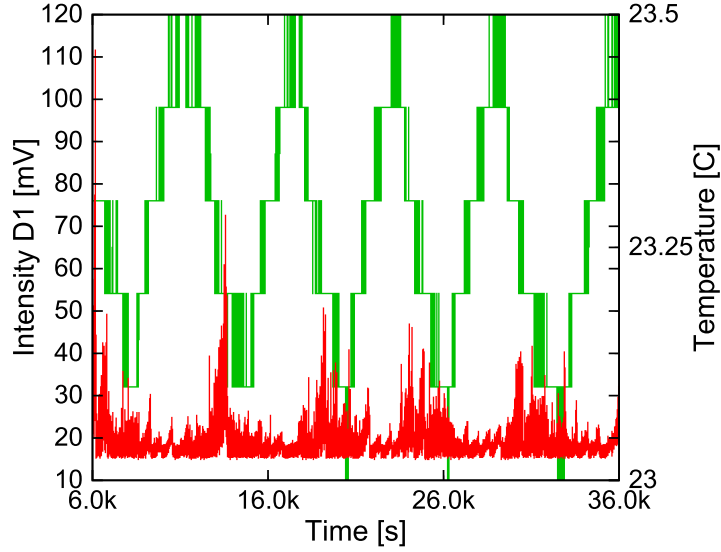


Figure 20: Relationship between phase fluctuations and laboratory temperature. Data related to D1 signal are denoted by red lines. Temperature data are denoted by green lines. The temperature curve have visible plateaus and jumps, but these are just artefacts caused by closeness of temperature resolution 0.1C° to the magnitude of temperature fluctuations.

To get more insight into the origin of phase fluctuations, the detection was extended by the temperature sensor. The temperature sensor is placed on the optical table approximately in the centre of the interferometer. The rest remains the same. A new run of the stability measurement is used to acquire more data. The Figure 20 shows that temperature in the lab was changing periodically with approximately same frequency as the phase. A part of data without significant irregularities, from $t = 6000\text{s}$ to $t = 36000\text{s}$, is used to further analysis. Both temperature and signal D1 data subsets are mapped to the interval $(0; 1)$. The mean value is subtracted in order to avoid large $\delta(f)$ -like peak in the spectrum origin. To evaluate the frequency spectrum, the Fast Fourier transform (FFT) is applied. Both spectra are normalized. To analyse correlations we calculated the spectral overlap $C = |\text{FT}[(I_{D1}(t))](f)| \cdot |\text{FT}[(T(t))](f)|$. The spectra are plotted in Figure 21 (a) and the spectral overlap in Figure 21 (b). The spectral peaks are overlapping at frequency $f = 166\ \mu\text{Hz}$ which corresponds to period of 1 hour and 40 minutes. This period matches the period of the air conditioning in the laboratory.

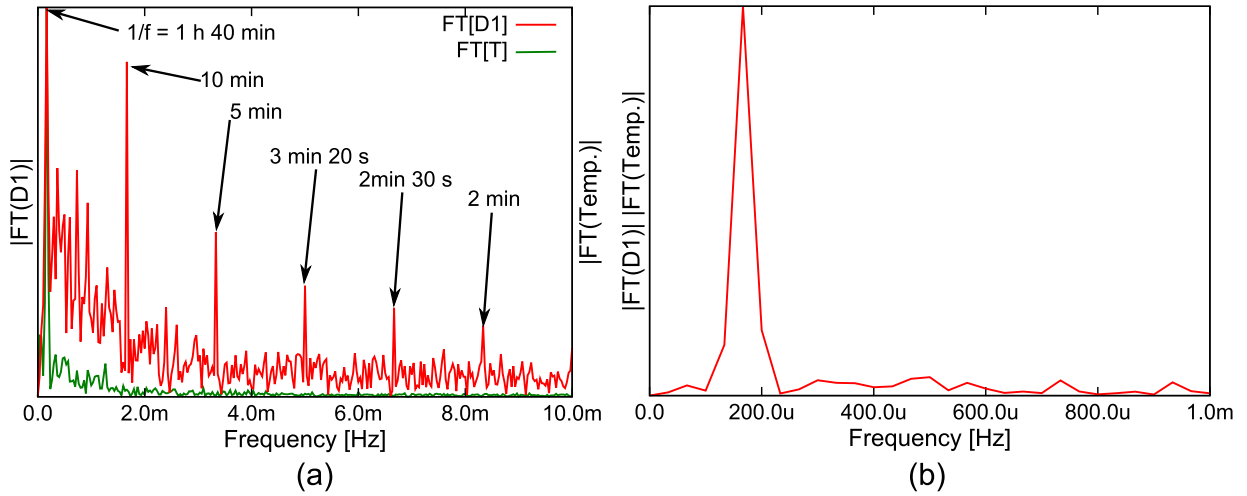


Figure 21: Spectra of the temperature and signal from detector D1. (a) Fourier transforms of the D1, denoted by the red curve, and the temperature data, denoted by the green curve. (b) Spectral overlap C . Both spectra have a significant peak at frequency $f = 166 \mu\text{Hz}$.

To conclude this section, the real-time phase stabilization of the MZ interferometer is not required for this proof of principle experiment. However, the output is influenced by phase fluctuations and therefore the gate operation can be affected.

4.2 Hofmann bound characterisation

The standard tool for characterisation of the experimental process is the fidelity, which measures the overlap between the actual process matrix χ and the desired process matrix χ_{CZ} . The process fidelity and the success probability of the CZ gate with weak coupling depend on the strength of the bypass channel, characterised by angle of HWPX ϕ_x . To show this dependence, we need to estimate the process fidelity for many settings of angle ϕ_x .

One way to obtain the fidelity is to perform full quantum process tomography, reconstruct the process matrix and directly use equation (20). That would be time-consuming, because the process tomography of the 2 qubit system requires 1296 measurements. The efficient way to estimate the lower bound of the process fidelity is introduced in article [12]. We call this method the Hofmann bound method. Only 32 measurements are required to estimate the lower Hofmann bound.

Assume two sets of states $S_1 = \{|0+\rangle, |0-\rangle, |1+\rangle, |1-\rangle\}$, $S_2 = \{|+0\rangle, |+1\rangle, |-0\rangle, |-1\rangle\}$. First we prepare i -th input state $|\psi\rangle_{ki}$ from set S_k and measure the projection of the gate output onto j -th state $|\psi\rangle_{kj} \in S_k$. The coincidence count rate is denoted by C_{kij} . This measurement is repeated for $k = 1, 2$ and i, j iterating over whole S_k set.

From the data set $\{C_{kij}\}$, the Hofmann bound is estimated as

$$F_H = F_1 + F_2 - 1 = \sum_{m=0}^3 (f_{1m} + f_{2m}) - 1 \quad (32)$$

with

$$f_{km} = \frac{C_{kmm}}{\sum_{i,j=0}^3 C_{kij}}. \quad (33)$$

The error is estimated using the law of error propagation

$$(\delta F_H)^2 \approx \sum_{k=1}^2 \sum_{i,j=0}^3 \left(\frac{\partial F_H}{\partial C_{kij}} \right)^2 (\delta C_{kij})^2. \quad (34)$$

The variance of the count rate $(\delta C_{kij})^2$ is same as its mean value C_{kij} , because the distribution of the count rate is approximately Poissonian.

The average success probability is

$$P_S = K \cdot \frac{1}{8} \sum_{k=1}^2 \sum_{i=0}^3 (p_{kii}), \quad (35)$$

where p_{kii} denotes the relative frequency of projection when input state is prepared in $|\psi\rangle_{ki} \in S_k$ and the output from the CZ gate is projected back to $|\psi\rangle_{ki}$. Value of p_{kii} is calculated from the experimental data by relation $p_{kii} = \frac{C_{kii}}{C_{\text{ref}}}$, where C_{ref} is the reference value measured as count rate of projection to $|00\rangle$ when prepared on the input $|00\rangle$ and the bypass is not used. The factor $K = 0.683$ represents joint intensity transmittance of PPBS and PPBSB.

We use again the law of error propagation to estimate the error

$$(\delta P_S)^2 \approx \sum_{k=1}^2 \sum_{i,j=0}^3 \left(\frac{\partial P_S}{\partial C_{kij}} \right)^2 (\delta C_{kij})^2 + \left(\frac{\partial P_S}{\partial C_{\text{ref}}} \right)^2 (\delta C_{\text{ref}})^2. \quad (36)$$

Variances $(\delta C_{kij})^2$ are known under assumption that the count rate distribution is approximately Poissonian.

To compare experimental results with the theoretical model, we need to express the Hofmann bound from the model output χ which is determined by equation (28). The lower bound of the fidelity is

$$F_\chi \geq F_H = F_1 + F_2 - 1. \quad (37)$$

The average output state fidelity F_k is

$$F_k = \frac{\sum_i p_{ki} f_{ki}}{\sum_i p_{ki}}, \quad (38)$$

where $p_{ki} = \text{Tr}[(|\psi\rangle_{ki}\langle\psi|_{ki} \otimes \mathbb{I})\chi]$ is the success probability and f_{ki} is fidelity of the actual output state with respect to the ideally expected state

$$f_{ki} = \frac{\text{Tr}[(|\psi\rangle_{ki}\langle\psi|_{ki} \otimes U_{CZ} |\psi\rangle_{ki}\langle\psi|_{ki} U_{CZ}^\dagger)\chi]}{\text{Tr}[(|\psi\rangle_{ki}\langle\psi|_{ki} \otimes \mathbb{I})\chi]}. \quad (39)$$

The average success probability is

$$P_S = \frac{1}{4} \text{Tr}[\chi]. \quad (40)$$

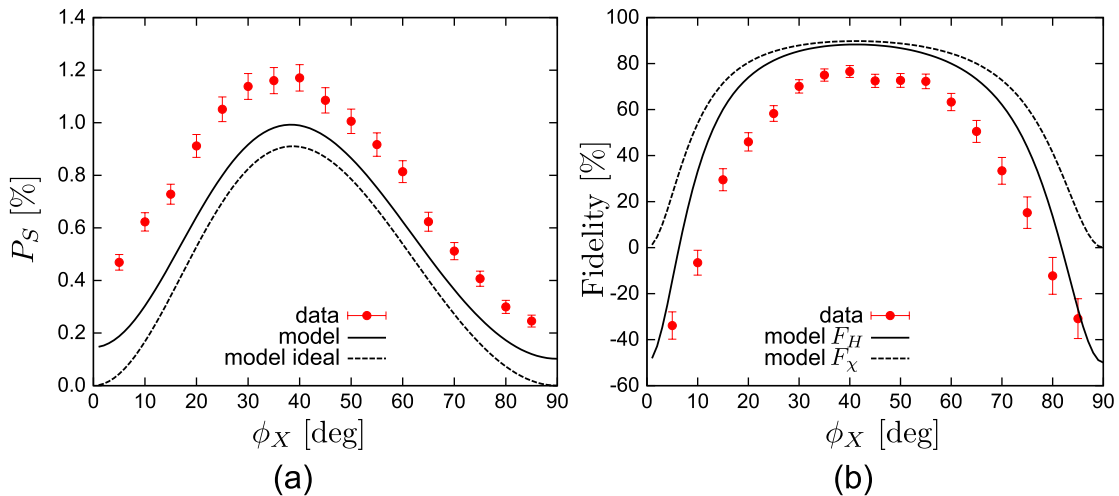


Figure 22: Characterisation of CZ gate for different coupling strength. (a) Success rate of the gate as a function of the bypass coupling strength. Red points with 3σ error-bars represent experimental results. Solid and dashed lines stand for theoretically predicted success probability for model with and without experimental imperfections, respectively. (b) Dependence of the fidelity on the strength of the bypass coupling characterised by angle of HWPX ϕ_x . Red points with 3σ error-bars show the experimental results. Solid line represents the theoretical prediction of the Hofmann lower bound F_χ . Dashed line shows predicted fidelity of the process F_χ . Both fidelities were calculated with respect to the ideal CZ process and with experimental imperfection of parasitic reflectance and partially distinguishable photons.

The price for restoring the CZ operation is the reduction of success probability. Achieved maximal success probability is lesser than $1/9$ for ideal CZ gate. The success probability is shown in Figure 22 (a). The maximal success probability predicted by the theoretical model without imperfections is $P_S = 0.91\%$ at coupling strength $\phi_X = 20^\circ$. This is the optimal bypass coupling strength for the CZ restoration. The dependence is plotted by dashed line. If we take imperfections into account, then the theoretical model predicts maximal success probability $P_S = 0.99\%$. This is depicted by the solid line. We measured even higher success probabilities, $P_{S,exp} = (1.17 \pm 0.02)\%$ at the optimal point. The increase of the success probability is caused by detection events for which the gate does not do the desired operation.

Figure 22 (b) includes comparison of the experimental results to the theoretical estimation of the process fidelity with respect to parameter ϕ_X . Ideally we should see a constant function $F_\chi = F_H = 1$ independent on ϕ_X . Due to experimental imperfections the fidelity is dependent on the coupling strength to the bypass mode. Please note, that the Hofmann bound estimation can be negative, since nothing guarantees $F_1 + F_2 \geq 1$. The process

fidelity is predicted by the theoretical model and plotted as the dashed line. The predicted process fidelity reaches $F_\chi = 0.898$ at the optimal bypass. The Hofmann lower bound is also predicted from the model and plotted as the solid line in (b). The predicted lower bound for optimal bypass is $F_H = 0.883$. The experimentally obtained lower bound is $F_{H,exp} = 0.765 \pm 0.009$ at the optimum and is lower than the lower bound prediction of the model because not every experimental imperfection is taken into account when calculating the theoretical model. For example, phase fluctuations and imperfection of wave plates were not taken into account.

4.3 Quantum process tomography

To illustrate the restoration of the CZ gate functionality in weak-coupling regime, we performed the full tomography with and without using the bypass channel of optimal strength.

Assume set of states $S_t = \{|0\rangle, |1\rangle, |+\rangle, |-\rangle, |R\rangle, |L\rangle\}$, where $|R\rangle = \frac{1}{\sqrt{2}}(|0\rangle + i|1\rangle)$ and $|L\rangle = \frac{1}{\sqrt{2}}(|0\rangle - i|1\rangle)$. In one measurement step we prepare input $|\psi\rangle_i|\psi\rangle_j$, where $|\psi\rangle_{i,j} \in S_t$. The output from the CZ gate is projected to state $|\psi\rangle_k|\psi\rangle_l$, where $|\psi\rangle_{k,l} \in S_t$. The measurement outcome is the coincidence count rate C_{ijkl} . We iterated each index over all six states in S_t and in the end collected data of 1296 coincidences. We took also 37 additional reference measurements. The input state is prepared in $|0\rangle|0\rangle$ state and the output is projected onto $|0\rangle|0\rangle$ state and HWPX, HWPY and HWPY are set to zero degrees for the reference measurement. The reference coincidence count rate is denoted as $C_{ref} := C_{0000}$ and the measured dataset is plotted in Figure 23.

The coincidences are accumulated over 10 s long interval. The average time to change the waveplates settings is 6.5 s. This yields approximately 6 hours for tomography consisting of 1333 data points.

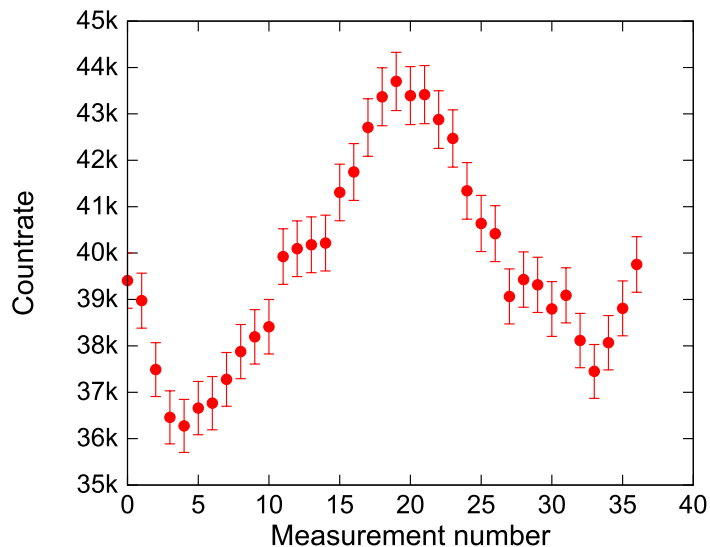


Figure 23: Reference coincidence count rates. Both qubits are prepared in $|0\rangle$ state and both outputs are projected onto $|0\rangle$. The error-bars represent 3σ assuming Poissonian distribution.

We assume that the count rate fluctuation is mainly caused by photon pair source instability. These fluctuations are partially compensated in analysis via proper scaling

with use of the reference and the linear interpolation. Let $C_{ref}(n)$ be n -th measurement of the reference. Compensated value of original count rate C_{ijkl} is

$$\bar{C}_{ijkl} := C_{ijkl} \frac{C_{ref}(0)}{C'_{ref}(i, j, k, l)}, \quad (41)$$

where indices go from 0 to 5 and

$$C'_{ref}(i, j, k, l) := \frac{C_{ref}(6i + j + 1) - C_{ref}(6i + j)}{36} (6k + l) + C_{ref}(6i + j) \quad (42)$$

is the linearly interpolated reference value.

Data are used to reconstruct the process matrix using the maximum likelihood estimation method [13]. Coincidences between APD2 and APD3 are used. In the reconstruction, we interchange $|+\rangle$ and $|-\rangle$ state on the input control qubit to obtain the expected result.

The reference count rate compensation plays only a negligible role in purity and fidelity of the reconstructed process. We achieved process purity $P = 0.859$ and process fidelity $F_\chi = 0.814$ for uncompensated data. With the compensation we achieved $P = 0.859$ and fidelity $F_\chi = 0.814$. The difference lies beyond the third decimal digit - $\Delta P = 0.0003$, $\Delta F_\chi = 3 \cdot 10^{-8}$. In this case, the compensation on the reference count rate fluctuation is not critical. The process matrix reconstructed from the compensated data is depicted in Figure 24.

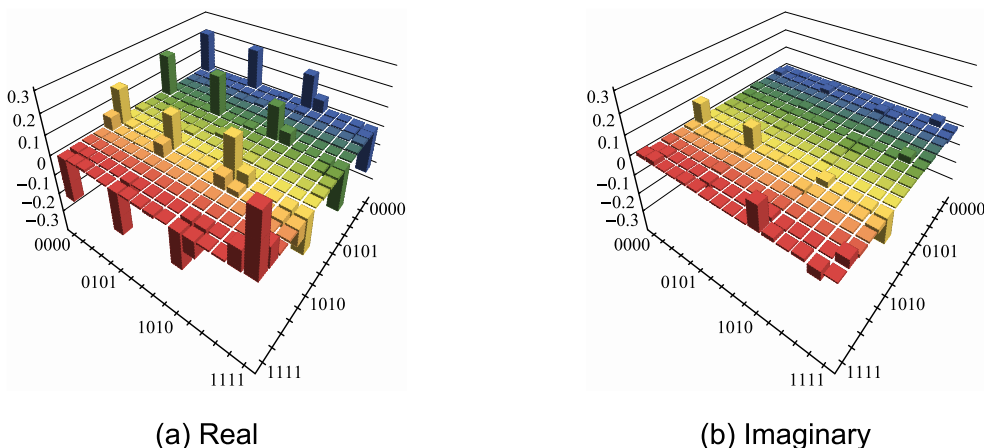


Figure 24: Reconstructed process matrix for optimal bypass. The reconstruction is calculated from compensated data.

We use Monte-Carlo approach to estimate the error of the measurement. We generate 100 datasets using Poissonian pseudo-random number generator, where the λ -parameter of the Poissonian distribution is taken from the original tomography data set. This can be understood as simulating 100 tomography measurements. Each dataset is processed using maximum likelihood reconstruction and process fidelity is calculated. From the set of these fidelities we calculate the mean value and one standard deviation. The process fidelity reached $F_\chi = 0.814 \pm 0.002$.

One can notice non-negligible elements in the imaginary part in comparison to the ideal CZ process matrix. These elements are caused by unwanted additional phase shifts. To compensate this we apply following post-process: we scan over additional phases φ_c and φ_t applied on output qubits of the gate to find the maximal fidelity of such process with respect to the ideal CZ process. The effect of phase shifts on output qubit of the gate is described by:

$$\chi_{new}(\varphi_c, \varphi_t) := [U_{ps}(\varphi_c) \otimes U_{ps}(\varphi_t)]\chi[U_{ps}(\varphi_c) \otimes (U_{ps}(\varphi_t))]^\dagger \quad (43)$$

with $U_{ps}(\varphi) := |0\rangle\langle 0| + \exp(i\varphi)|1\rangle\langle 1|$. The dependence of the process fidelity on additional output phase shifts is plotted in Figure 25. With the optimal phase shifts we are able to reduce the imaginary contribution in the χ matrix and increase the fidelity to $F_\chi = 0.846$.

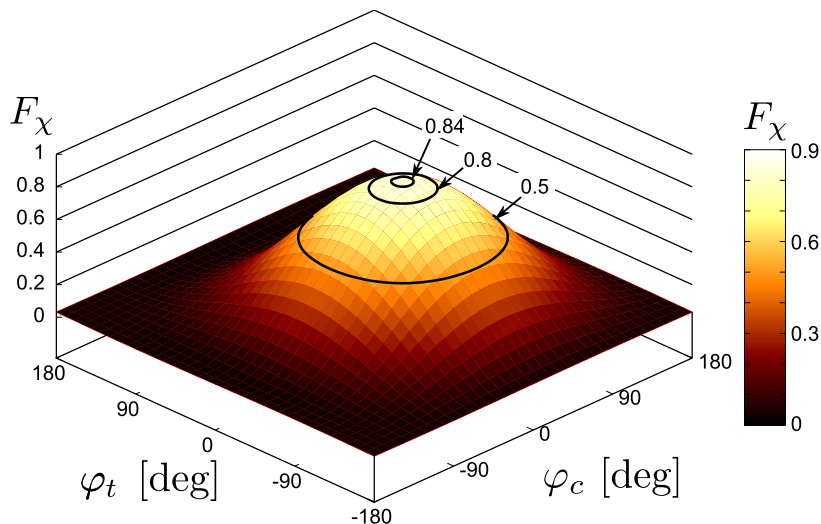


Figure 25: Dependence of fidelity of the reconstructed process with respect to ideal CZ process on additional phase shift on outputs. The maximum is $F_\chi = 0.846$ at $\varphi_c = 14^\circ, \varphi_t = -18^\circ$.

Figure 26 depicts the reconstructed process matrix of the device without bypass (a), with optimal bypass and phase shift correction (b) and the ideal CZ process matrix (c). In the Figure, one can compare (a) and (c) to find out, that without the bypass channel, the CZ operation in weak-coupling regime is lost and we get an identity operation up to unequal attenuation of modes. On the other hand, when we use the optimal bypass, the CZ operation is restored regardless the weak coupling.

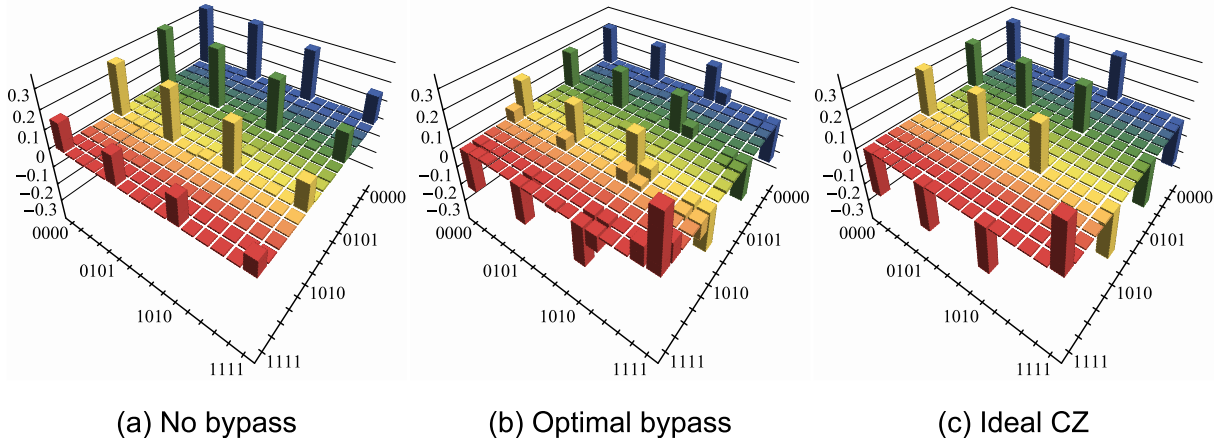


Figure 26: (a) reconstructed process matrix of the device without using bypass channel, (b) reconstructed process matrix of the device in optimal bypass regime, which is close to ideal CZ process (c). Only real parts are plotted.

The process fidelity F_χ is a suitable tool for comparing closeness of the implemented operation to the ideal one within systems of the same class and dimension. The fidelity itself does not provide much insight into the process. One can perform more observations on the reconstructed process matrix. Here we would like to demonstrate entangling capabilities of the implemented gate by means of data post-processing. It is known that CZ gate is capable of preparing maximally entangled states. The input state $|++\rangle$ is transformed by ideal CZ gate and Hadamard transform on the output target qubit, into the Bell state

$$|\Phi^+\rangle := \frac{1}{\sqrt{2}} (|00\rangle + |11\rangle). \quad (44)$$

One can measure the entanglement of the state using the logarithmic negativity

$$N(\rho) := \log_2 \left(\text{Tr} \sqrt{(\rho^{T_a})^\dagger \rho^{T_a}} \right), \quad (45)$$

where ρ is the evaluated density matrix and symbol T_a denotes the partial transposition over the first part of the system.

The logarithmic negativity of the mentioned Bell state $|\Phi^+\rangle$ is

$$N(|\Phi^+\rangle\langle\Phi^+|) = 1$$

and we say that the state is maximally entangled. From the reconstructed process matrix χ , one can predict the output state for given input ρ_{in} by using relation

$$\rho_{out} := \text{Tr}_{in}[(\rho_{in} \otimes \mathbb{I})\chi], \quad (46)$$

where Tr_{in} stands for the partial trace over the input part of the matrix.

Applying the $|++\rangle$ state as an input to the reconstructed CZ χ matrix and using equation (46) we obtain the output ρ_{out} . Hadamard operation of the output target qubit of ρ_{out} provides a new state

$$\rho_{out2} := (\mathbb{I} \otimes U_H)\rho_{out}(\mathbb{I} \otimes U_H)^\dagger$$

which should produce the Bell state. The logarithmic negativity is $N(\rho_{out2}) = 0.862$. The purity of the output state provided by our gate is estimated to be $P = 0.894$. To quantify similarity of the density matrices ρ_1 and ρ_2 we use the state fidelity $F(\rho_1, \rho_2) := [\text{Tr}\sqrt{\sqrt{\rho_1}\rho_2\sqrt{\rho_1}}]^2$. The fidelity is $F(\rho_{out2}, |\Phi^+\rangle\langle\Phi^+|) = 0.905$. The Figure 27 shows the predicted output based on reconstructed χ matrix.

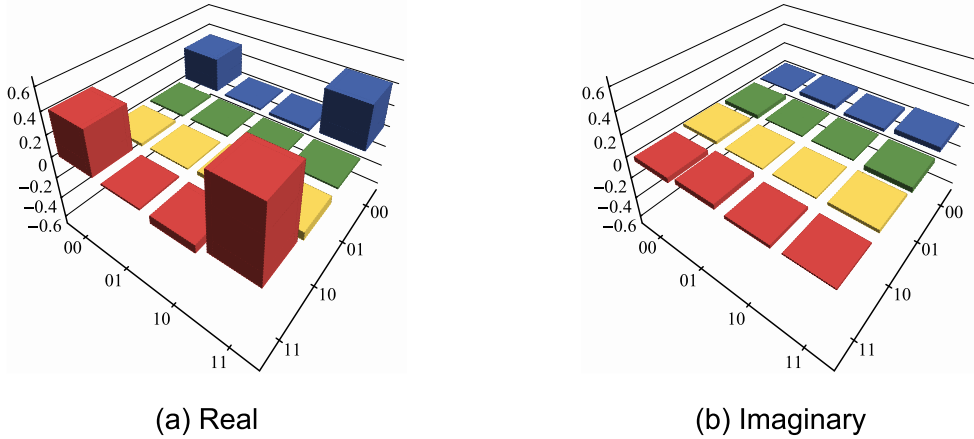


Figure 27: Prediction of the Bell state output. When the Hadamard transform and the correct input state is applied, we should see Bell state $|\Phi^+\rangle$ on the output. The figure shows the estimation of output density matrix produced by our gate.

5 Summary

A weak coupling between two physical systems might be an obstacle for quantum gate construction. In this thesis we overcome this limitation in the context of quantum control-Z gate. We introduced a new method based on coupling one qubit to auxiliary mode and thus partly avoiding interaction itself. The quantum interference, filtering and coincidence post selection have been used to enhance the coupling between two physical systems.

We experimentally demonstrated the restoration of control-Z operation between two weakly coupled single-photon qubits using linear quantum optics. Although the weak coupling is generally not a problem in linear quantum optics we use this platform as a testbed for our method. Target qubits were encoded into polarization mode and control qubits were encoded into spatial modes of the Mach-Zehnder interferometer. Therefore the phase stability of the Mach-Zehnder interferometer was measured and data from the measurement were processed using Allan deviation. On time scale of tomography measurement the phase Allan deviation is 7.7° . We showed by means of Fourier analysis that phase fluctuations were related to the temperature in the laboratory. Although the maximal phase shift reached 40° , the active stabilization was not required for our demonstration.

The weak coupling was implemented by convenient choice of the beam splitter parameters in the setup. We took experimental imperfections of parasitic reflectance r_H of the beam splitter and the partial distinguishability of the photons into account of our theoretical model. We showed that these imperfections causes the dependence of the process fidelity on the bypass strength. These imperfections limited the maximally achievable process fidelity to $F_\chi = 0.898$.

The dependence of the bypass coupling strength on the process fidelity and success probability was characterised using the Hofmann bound method. Also a optimal bypass strength was found with the success probability reaching 1.17%. The reduction of the success probability was the price for the restoration of the control-Z gate in weak coupling regime. At the point of optimal bypass we demonstrated the CZ process restoration using the quantum process tomography. The process matrix was reconstructed using the maximum likelihood method and the process fidelity was $F_\chi = 0.814$. By post-processing we showed that the process fidelity can be increased to $F_\chi = 0.846$ by applying phase shifts on the gate outputs. We also showed entangling capabilities of the implemented control-Z gate and the logarithmic negativity reached 0.862.

We hope that the presented method might be valuable for implementing gates on systems that suffer from weak coupling, decoherence or the control over the one subsystem is limited.

6 Bibliography

- [1] MIT, “Information and entropy - course materials,” (2003).
- [2] M. Nielsen and I. Chuang, *Quantum Computation and Quantum Information: 10th Anniversary Edition* (Cambridge University Press, 2010).
- [3] N. Kiesel, C. Schmid, U. Weber, R. Ursin, and H. Weinfurter, Phys. Rev. Lett. **95**, 210505 (2005).
- [4] N. K. Langford, T. J. Weinhold, R. Prevedel, K. J. Resch, A. Gilchrist, J. L. O’Brien, G. J. Pryde, and A. G. White, Phys. Rev. Lett. **95**, 210504 (2005).
- [5] R. Okamoto, H. F. Hofmann, S. Takeuchi, and K. Sasaki, Phys. Rev. Lett. **95**, 210506 (2005).
- [6] T. Monz, K. Kim, W. Hänsel, M. Riebe, A. S. Villar, P. Schindler, M. Chwalla, M. Hennrich, and R. Blatt, Phys. Rev. Lett. **102**, 040501 (2009).
- [7] K. Hammerer, A. S. Sørensen, and E. S. Polzik, Rev. Mod. Phys. **82**, 1041 (2010).
- [8] D. G. Cory, M. D. Price, W. Maas, E. Knill, R. Laflamme, W. H. Zurek, T. F. Havel, and S. S. Somaroo, Phys. Rev. Lett. **81**, 2152 (1998).
- [9] E. Knill, R. Laflamme, and G. J. Milburn, Nature **409**, 46 (2001).
- [10] M. Mičuda, M. Sedlák, I. Straka, M. Miková, M. Dušek, M. Ježek, and J. Fiurášek, Phys. Rev. Lett. **111**, 160407 (2013).
- [11] D. Allan, Proceedings of the IEEE **54**, 221 (1966).
- [12] H. F. Hofmann, Phys. Rev. Lett. **94**, 160504 (2005).
- [13] M. Paris and J. Řeháček, *Quantum State Estimation*, Lecture Notes in Physics (Springer, 2004).

A Derivations

Used symbolic:

The symbol $O_1 \xrightarrow{\text{component}} O_2$ denotes transformation of operator O_1 by a component which results in operator O_2 . In this section we omit \dagger symbol in creation operators to keep the nomenclature simple. We also often skip writing the kets of states, instead we write only creation operators.

(a) CZ concept:

Input $|00\rangle$ is attenuated at BS_A, BS_B

$$a_0 b_0 \xrightarrow{\text{BSA,BSB}} t_a t_b a_0 b_0.$$

For input $|01\rangle$ the transformation reads

$$a_0 b_1 \xrightarrow{\text{BS,BSA}} t t_b a_0 b_1 - r t_b a_0 b_0.$$

Here we use fact, that coincidence measurement (CC) accepts only cases when photons are in each qubit

$$t t_b a_0 b_1 - r t_b a_0 a_1 \xrightarrow{\text{CC}} t t_b a_0 b_1.$$

Similarly $|10\rangle$ on the input

$$a_1 b_0 \xrightarrow{\text{BS,BSB}} t t_b a_1 b_0 + r t_b b_1 b_0 \xrightarrow{\text{CC}} t t_b a_1 b_0.$$

Input $|11\rangle$ is transformed by

$$a_1 b_1 \xrightarrow{\text{BS}} (a_1 t + r b_1)(b_1 t - a_1 r) \xrightarrow{\text{CC}} (t^2 - r^2) a_1 b_1.$$

The condition on same size of the output amplitudes $t_a t_b = t_a t = t_b t$ is satisfied when $t_a = t_b = t$. The condition $t_b t = R - T$ can be rewritten as $1 - 2t^2 = t^2$. These equations are satisfied when $t = t_a = t_b = \frac{1}{\sqrt{3}}$.

(b) wCZ concept:

The scheme is calculated similarly as in previous case and therefore the derivation is provided without further comments.

Input $|00\rangle$

$$a_0 b_0 \xrightarrow{\text{BSA,BSB}} t_a t_b a_0 b_0.$$

Input $|01\rangle$

$$a_0 b_1 \xrightarrow{\text{BSA,BS}} t_a t a_0 b_1.$$

Input $|10\rangle$

$$\begin{aligned} a_1 b_0 &\xrightarrow{\text{BSX,BSB}} t_b b_0 (t_x a_1 + r_x c) \xrightarrow{\text{BS}} t_b b_0 [t_x (t a_1 + r b_1) + r_x c] \xrightarrow{\text{CC}} \\ &t_b b_0 [t_x t a_1 + r_x c] \xrightarrow{\text{BSY}} t_b b_0 [t_x t t_y a_1 + r_y r_x c] = t_b (t t_x t_y + r_x r_y) a_1 b_0. \end{aligned}$$

Input $|11\rangle$

$$\begin{aligned} a_1 b_1 &\xrightarrow{\text{BSX}} (t_x a_1 + r_x c) b_1 \xrightarrow{\text{BS}} [t_x (t a_1 + r b_1) + r_x c] (t b_1 - r a_1) \xrightarrow{\text{CC}} (t^2 - r^2) t_x a_1 b_1 + r_x t c b_1 \\ &\xrightarrow{\text{BSY}} [(t^2 - r^2) t_x t_y + r_y r_x t] a_1 b_1 = [(2t^2 - 1) t_x t_y + r_x r_y t] a_1 b_1. \end{aligned}$$

Size of amplitudes must be equal and the fourth amplitude has to have the opposite sign in order to restore the CZ operation. Putting the first two output amplitudes equal implies

$$t_a t = t_a t_b \iff t = t_b.$$

The second and the third amplitude have also to be equal

$$t_a t_b = t_b (t t_x t_y + r_x r_y) \iff t_a = t t_x t_y + r_x r_y.$$

Finally, negatively taken fourth amplitude has to be equal to the third amplitude. Together with $t = t_b$ we have

$$-[(2t^2 - 1) t_x t_y + r_x r_y t] = t (t t_x t_y + r_x r_y),$$

which is divided $r_x r_y$ to obtain

$$\frac{t_x t_y}{r_x r_y} = \frac{2t}{1 - 3t^2}.$$

The first and the third amplitude have to be equal

$$t_a t_b = t (t t_x t_y + r_x r_y).$$

Together with the condition on phase shift we have

$$t (t t_x t_y + \frac{1 - 3t^2}{2t} t_x t_y) = \frac{1}{2} t_x t_y (1 - t^2) = \frac{1}{2} t_x t_y R.$$

Therefore the success probability is

$$P_S = \frac{1}{4}t_x^2 t_y^2 R^2.$$

(c) wCZ - maximal success probability condition:

We are trying to find the maximum of probability

$$P_S(t_x, t_y) = \frac{1}{4}T_x T_y (1 - t^2)^2$$

with the constraint

$$\frac{t_x t_y}{r_x r_y} = \frac{2t}{1 - 3t^2}.$$

The constraint can be rewritten for purpose of the Lagrange multipliers method as

$$G(T_x, T_y) := \left[1 - \left(\frac{2t}{1 - 3t^2} \right)^2 \right] T_x T_y + \left(\frac{2t}{1 - 3t^2} \right)^2 (T_x + T_y - 1) = 0,$$

where we defined $T_{x,y} := t_{x,y}^2$ and used the fact that $1 - T_{x,y} = R_{x,y}$. Now we can insert the function P_s and constraint G into Lagrange equations

$$\begin{aligned} \frac{\partial P_s}{\partial T_x} - \lambda \frac{\partial G}{\partial T_x} &= 0, \\ \frac{\partial P_s}{\partial T_y} - \lambda \frac{\partial G}{\partial T_y} &= 0, \\ G &= 0. \end{aligned}$$

From first two equations in the system, we obtain $T_x = T_y$. Then we can reduce system to two equations of two variables:

$$\begin{aligned} \frac{1}{2}T_x(1 - t^2) - 2\lambda(1 - \left(\frac{2t}{1-3t^2}\right)^2)T_x - 2\lambda\left(\frac{2t}{1-3t^2}\right)^2 &= 0 \\ (1 - \left(\frac{2t}{1-3t^2}\right)^2)T_x^2 + 2\left(\frac{2t}{1-3t^2}\right)^2 T_x - \left(\frac{2t}{1-3t^2}\right)^2 &= 0 \end{aligned}$$

which we solve in Wolfram Mathematica for T_x and λ to obtain two solutions $T_x = \frac{2t}{2t+1-3t^2}$ and $T_x = \frac{2t}{2t-1+3t^2}$.

Solutions can be written as

$$T_x = t_x^2 = \frac{2t}{2t + |1 - 3t^2|}.$$

for which the probability is maximized.

(d) wCZ implementation - function of blocks:

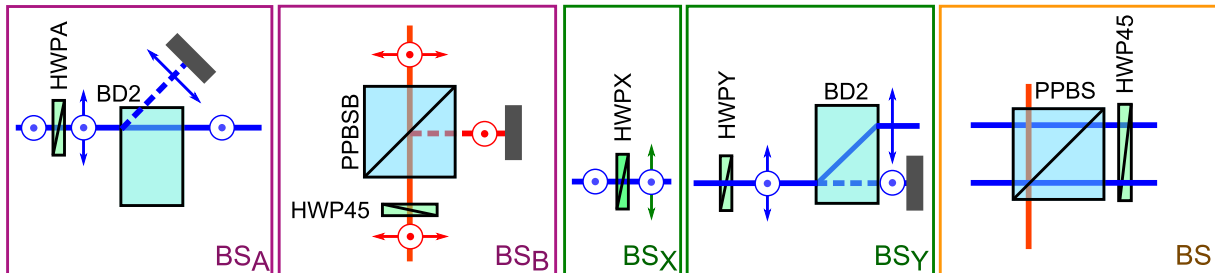


Figure 28: Building blocks for our implementation of CZ gate. Where possible, polarization effects are illustrated by arrow marks.

As a step one to calculation of our implementation, it is convenient to break down the gate into building blocks, illustrated in Figure 28, and describe each block separately. We took coincidence logic and filtering properties of some components into account.

HWP45 together with PPBSB acts as an attenuator for horizontally polarized component of the input field. The half-wave plate at angle 45 degrees turns horizontally polarized component into vertically polarized component and vice versa. Light reflected from PPBSB does not reach any detector and thus we don't take reflected modes into account. Therefore the transformation is

$$\begin{aligned} b_H &\xrightarrow{\text{BSB}} b_V t, \\ b_V &\xrightarrow{\text{BSB}} b_H t_H. \end{aligned} \quad (47)$$

Similarly, BS_A attenuates mode U_V by changing the angle of linear polarization and subsequent reflection of horizontally polarized light, which does not reach any detector. To get the correct phase we introduce angle $\phi_a := \pi - \phi'_a$, where ϕ'_a is actual angle of the HWP45. This substitution is also applied in case of HWPX and HWPY. This is described by

$$u_V \xrightarrow{\text{BS}_A} \cos(2\phi_a)u_V := t_a u_V. \quad (48)$$

To achieve coupling into auxiliary bypass mode, BS_X block is used. HWPX provides coupling between horizontally-polarized and vertically-polarized mode of the bottom arm of the interferometer. The transformation is

$$\begin{aligned} d_H &\xrightarrow{\text{BS}_X} -\cos(2\phi_x)d_H + \sin(2\phi_x)d_V := -t_x d_H + r_x d_V, \\ d_V &\xrightarrow{\text{BS}_X} \cos(2\phi_x)d_V + \sin(2\phi_x)d_H := t_x d_V + r_x d_H. \end{aligned} \quad (49)$$

BS_Y provides projection of auxiliary bypass mode into control qubit. The transformation

is

$$\begin{aligned} d_H &\xrightarrow{\text{BSY}} \cos(2\phi_y)u_H := t_y u_H, \\ d_V &\xrightarrow{\text{BSY}} \sin(2\phi_y)u_H := r_y u_H. \end{aligned} \quad (50)$$

Central beam splitter (BS) is described by transformation relations

$$\begin{aligned} u_H b_H &\xrightarrow{\text{BS}} u_V b_H t_H^2, \\ u_H b_V &\xrightarrow{\text{BS}} u_V b_V t_H t, \\ d_H b_H &\xrightarrow{\text{BS}} d_V b_H (t_H^2 - r_H^2), \\ d_H b_V &\xrightarrow{\text{BS}} d_V b_V t_H t - d_H b_H r_H r, \\ d_V b_H &\xrightarrow{\text{BS}} d_H b_H t_H t - d_V b_V r_H r, \\ d_V b_V &\xrightarrow{\text{BS}} d_H b_V (t^2 - r^2). \end{aligned} \quad (51)$$

In the following part we will describe the transformation effect of the CZ gate on input states: $|00\rangle$, $|01\rangle$, $|10\rangle$ and $|11\rangle$ for case of indistinguishable photons. The transformation relation mentioned before are used to perform the computation. Computations are provided without further comments.

$|00\rangle$

$$u_H b_H \xrightarrow{\text{BS}} u_V b_H t_H^2 \xrightarrow{\text{BSB}} u_V b_V t_H^2 t \xrightarrow{\text{BSA}} u_V b_V [t_A t_H^2 t].$$

$|01\rangle$

$$u_H b_V \xrightarrow{\text{BS}} u_V b_V t_H t \xrightarrow{\text{BSB}} u_V b_H t_H^2 t \xrightarrow{\text{BSA}} u_V b_H [t_A t_H^2 t].$$

$|10\rangle$

$$\begin{aligned} d_V b_H &\xrightarrow{\text{BSX}} t_X d_V b_H + r_X b_H d_H \xrightarrow{\text{BS}} t_X t_H t d_H b_H - t_X r_H r d_V b_V + r_X (t^2 - r^2) d_V b_H \\ &\xrightarrow{\text{BSB}} t_X t_H t^2 d_H b_V - t_X r_H r t_H d_V b_H + r_X (t_H^2 - r_H^2) t d_V b_V \\ &\xrightarrow{\text{BSY}} t_X t_Y t_H t^2 u_H b_H - t_X r_H t_H r d_V b_H + r_X (t_H^2 - r_H^2) t r_Y u_H b_V \\ &= u_H b_V [t_X t_Y t_H t^2 + r_X r_Y (t_H^2 - r_H^2) t] - u_H b_H [t_X r_Y r_H t_H r]. \end{aligned}$$

$|11\rangle$

$$\begin{aligned} d_V b_V &\xrightarrow{\text{BSX}} t_X d_V b_V + r_X d_H b_V \xrightarrow{\text{BS}} t_X (t^2 - r^2) d_H b_V + r_X t_H t d_V b_V - r_X r_H r d_H b_H \\ &\xrightarrow{\text{BSB}} t_X t_H (t^2 - r^2) d_H b_H + r_X t_H^2 t d_V b_H - r_X r_H t r d_H b_V \\ &\xrightarrow{\text{BSY}} t_X t_Y t_H (t^2 - r^2) u_H b_H + r_X r_Y t_H^2 t u_H b_H - t_Y r_X r_H t r u_H b_V \end{aligned}$$

$$= u_H b_H [t_X t_Y (t^2 - r^2) + r_X r_Y t_H^2 t] - u_H b_V [t_Y r_X r_H r t].$$

We will similarly write effect of the gate on distinguishable photons which undergoes double transmission. The transformation of the central beam splitter reduces to BS_{tt}

$$\begin{aligned} u_H b_H &\xrightarrow{\text{BS}} u_V b_H t_H^2, \\ u_H b_V &\xrightarrow{\text{BS}} u_V b_V t_H t, \\ d_H b_H &\xrightarrow{\text{BS}} d_V b_H t_H^2, \\ d_H b_V &\xrightarrow{\text{BS}} d_V b_V t_H t, \\ d_V b_H &\xrightarrow{\text{BS}} d_H b_H t_H t, \\ d_V b_V &\xrightarrow{\text{BS}} d_H b_V t^2. \end{aligned} \tag{52}$$

Again without further comments, transformation relations are:

|00⟩

$$u_H b_H \xrightarrow{\text{BS}} t_H^2 u_V b_H \xrightarrow{\text{BSB}} t_H^2 t u_V b_V \xrightarrow{\text{BSA}} u_V b_V [t_A t_H^2 t]$$

|01⟩

$$u_H b_V \xrightarrow{\text{BS}} t_H t u_V b_V \xrightarrow{\text{BSB}} t_H^2 t u_V b_H \xrightarrow{\text{BSA}} u_V b_H [t_A t_H^2 t].$$

|10⟩

$$\begin{aligned} d_V b_H &\xrightarrow{\text{BSX}} t_X d_V b_H + r_X d_H b_H \xrightarrow{\text{BS}} t t_X t_H d_H b_H + r_X t_H^2 d_V b_H. \\ &\xrightarrow{\text{BSB}} t_X t_H t^2 d_H b_V + r_X t_H^2 t d_V b_V \xrightarrow{\text{BSY}} t_Y t_X t_H t^2 u_H b_V + r_Y r_X t_H^2 t u_H b_V \\ &= u_H b_V t_X t_Y t_H t^2 + r_X r_Y t_H^2 t \end{aligned}$$

|11⟩

$$\begin{aligned} d_V b_V &\xrightarrow{\text{BSX}} t_X d_V b_V + r_X d_H b_V \xrightarrow{\text{BS}} t_X t^2 d_H b_V + r_X t_H t d_V b_V \\ &\xrightarrow{\text{BSB}} t_X t_H t^2 d_H b_H + r_X t_H^2 t d_V b_H \xrightarrow{\text{BSY}} t_Y t_X t_H t^2 u_H b_H + r_X r_Y t_H^2 t u_H b_H \\ &= u_H b_H t_X t_Y t_H t^2 + r_X r_Y t_H^2 t. \end{aligned}$$

The same calculation is done for case of two distinguishable photons that undergoes

double reflection on the central beam splitter

$$\begin{aligned}
u_H b_H &\xrightarrow{\text{BS}} 0, \\
u_H b_V &\xrightarrow{\text{BS}} 0, \\
d_H b_H &\xrightarrow{\text{BS}} -r_H^2 d_V b_H, \\
d_H b_V &\xrightarrow{\text{BS}} -r_H r d_H b_H, \\
d_V b_H &\xrightarrow{\text{BS}} -r_H r d_V b_V, \\
d_V b_V &\xrightarrow{\text{BS}} -r^2 d_H b_V.
\end{aligned} \tag{53}$$

|10⟩

$$\begin{aligned}
&d_V b_H \xrightarrow{\text{BSX}} t_X d_V b_H + r_X d_H b_H \xrightarrow{\text{BS}} -t_X r_H r d_V b_V - r_X r_H^2 d_V b_H \\
&\xrightarrow{\text{BSB}} -t_X t_H r_H r d_V b_H - r_X r_H^2 t d_H b_H \xrightarrow{\text{BSY}} -t_X r_Y t_H r_H r u_H b_H - r_X r_Y r_H^2 t u_H b_V \\
&= -u_H b_V [r_X r_Y r_H^2 t] - u_H b_H [t_X r_Y r_H t_H r]
\end{aligned}$$

|11⟩

$$\begin{aligned}
&d_V b_V \xrightarrow{\text{BSX}} t_X d_V b_V + r_X d_H b_V \xrightarrow{\text{BS}} -t_X r^2 d_H b_V - r_X r_Y r d_H b_H \\
&\xrightarrow{\text{BSB}} -t_X t_H r^2 d_H b_H - r_X r_H r t d_H b_V \xrightarrow{\text{BSY}} -t_X t_Y t_H r^2 u_H b_H - r_X t_Y r_H r t u_H b_V \\
&= -u_H b_H [t_X t_Y t_H r^2] - u_H b_V [r_X t_Y r_H r t]
\end{aligned}$$

Inputs |00⟩ and |01⟩ do not produce any coincidences.

B Custom USB voltmeter

The motivation for building the custom voltmeter was the equipment availability in our laboratory. Voltmeters are typically not designed for data acquisition at higher sampling rates. On the other hand, oscilloscopes provide very high sampling rate but they are not suitable for logging days-long data. We tried to fill this gap by a custom device.

For the similar purposes, the TTI1906 voltmeter is used in our laboratory. The first inconvenience was the serial-communication stability of the device. When one repeats the measurement with sufficient frequency and for sufficiently long time, the amount of serial-communication errors increases. This required extra error and exception-handling code in our scripts. The other inconvenience was the port consumption. One RS232 port per channel. The third inconvenience was the power socket usage - one power socket per channel. The fourth problem was the speed of the device - the samples per seconds (SPS) rate and the problem of numbers that sometimes got stuck in the serial buffer. The SPS rate could be 0.5 SPS for short times but on longer timescale 0.25 SPS was more stable.

In order to overcome this technical hurdle, we used an analog-to-digital converter (ADC) chip and a microcontroller. We chose the Arduino as a development platform, because it provided good documentation and comprehensible code.

For purpose of the phase stability characterisation we used Microchip MCP3424 sigma-delta ADC which provided 18-bit resolution at voltage range ± 2048 mV. The achieved sampling rate was 0.5 SPS which is comparable to TTI1906, but more stable. During the the several days long measurement we did not encountered single serial communication error.

Later, we used a pair of TI ADS1115 ADC, which provided 16-bit resolution at maximal rate 860 SPS. The Arduino facilitated the I2C communication with the ADC chip and serial communication with the computer. The voltage range was limited to 0-5 V by supply voltage, but higher voltage can be measured using built-in programmable amplifier with gain lesser than one. Similarly we could increase resolution for lower voltages. This limit was not problem for us because we commonly use DET36A/M PIN diodes which can reasonably operate in these boundaries. Each chip provided two differential channels, that is four in total. The electronics is depicted in Figure 29 and the physical appearance in Figure 30.

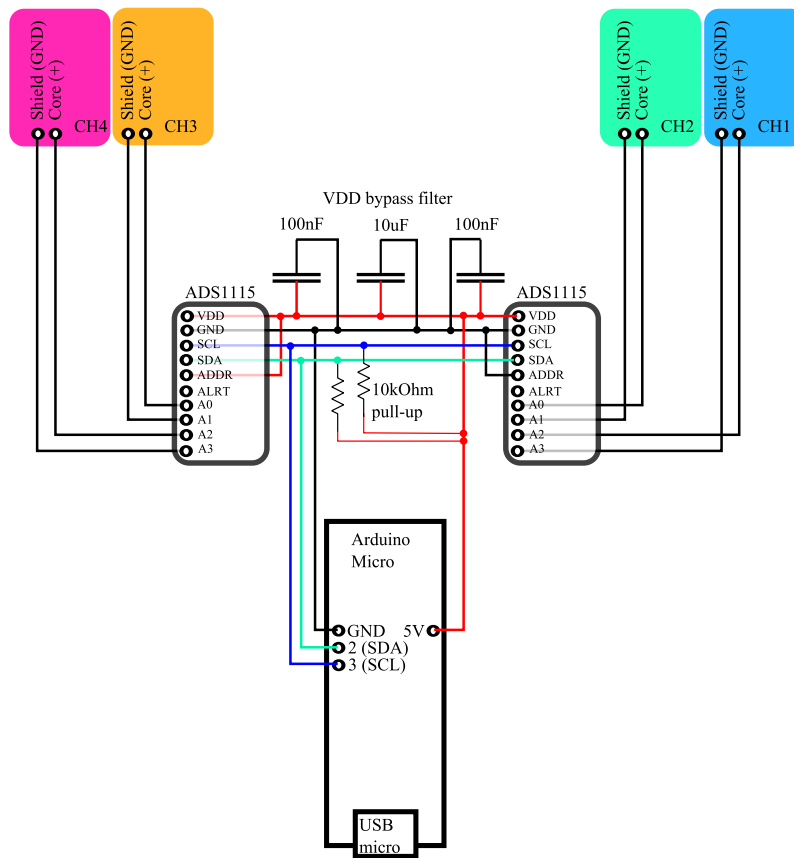


Figure 29: ADC-to-Arduino connection. I2C bus connected to SCL and SDA of the Arduino and both lines are connected via pull-up resistor to 5V voltage level. Power inputs of the chip are filtered using bypass capacitors. Connection of address pin sets the address of the ADC chip on I2C bus. ADC inputs are connected to BNC connectors in order to make the voltmeter box compatible with our coaxial cables ended with BNC connectors.

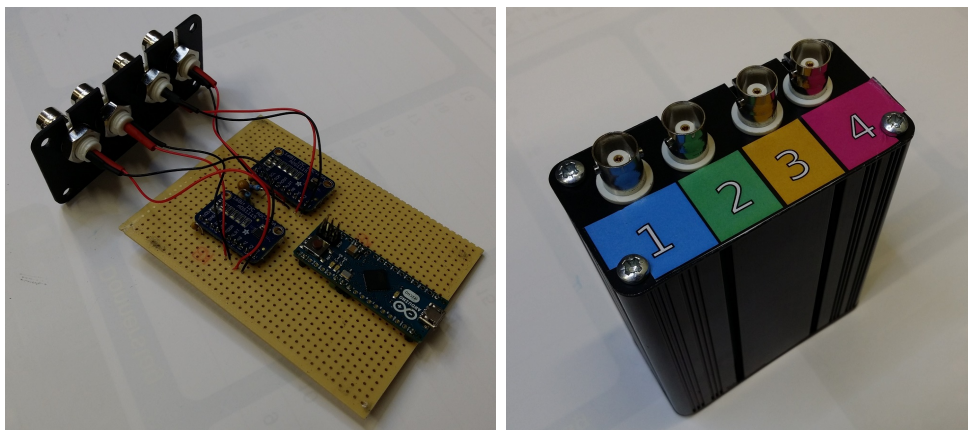


Figure 30: Physical appearance of the voltmeter. Left: development board, right: encapsulated in metal chassis.

The software kit we wrote consisted of three layers - Arduino code, Python module and graphics user interface (GUI). The first layer, the Arduino program is basically the communication protocol which takes the one-byte command and lets the ADC perform reading and returns 16 bit number as 2 bytes over the serial bus. This layer is built upon a modified library by Adafruit, where we fixed few inconsistencies and minor bugs.

The second layer, the Python module encapsulates serial communications and interpretation of incoming numbers into a single object. To obtain the voltage reading, one only has to know the serial port address and then getting numbers from ADS is as simple as for example:

```
1 | from ADS1115Quad import ADS1115Quad #import module
2 | ADC = ADS1115Quad("/dev/ttyACM1") #create instance and connect to
   | the device
3 | #later in code...
4 | CH1_voltage, CH3_voltage = ADC((1,0,1,0)) #read values
5 | #or simply (for channel 1):
6 | CH1_voltage = ADC()
```

The third layer is the GUI utility built on Python Qt. It used a second layer to communicate with the device. The motivation for GUI was to have numbers on a computer screen in large, clear and bright numbers as well as the real-time plotting values from the ADC. It made our adjustments more convenient.

To compare the result with the commonly used TTI1906, we have 4 channels on 1 USB. We can practically achieve effectively 240 SPS (60 on each channel, the SPS rate was limited to find a reasonable balance with the linearity of the ADC) and is stable in long-term measurements. The box does not require any additional power supply, just USB and fits into palm.